PREDICTING INTERFACIAL CHARACTERISTICS DURING POWDER BED FUSION PROCESS

PREDICTING INTERFACIAL CHARACTERISTICS DURING POWDER BED FUSION PROCESS

BY

PRABHAKAR PAL, B.Tech.

A THESIS

SUBMITTED TO THE DEPARTMENT OF MATERIALS SCIENCE AND ENGINEERING

AND THE SCHOOL OF GRADUATE STUDIES

OF MCMASTER UNIVERSITY

IN PARTIAL FULFILMENT OF THE REQUIREMENTS

FOR THE DEGREE OF

MASTER OF APPLIED SCIENCE

Master of Science (2022) McMaster University

(Materials Science and Engineering) Hamilton, Ontario, Canada

TITLE:	Predicting Interfacial Characteristics during Powder Bed Fusion Process
AUTHOR:	Prabhakar Pal B. Tech. (Mechanical Engineering), Indian Institute of Technology Bombay, Mumbai, India
SUPERVISOR:	Prof. André B. Phillion
NUMBER OF PAGES:	xxii, 116

Abstract

Powder bed fusion (PBF) is a metal additive manufacturing process that is increasingly used in the aerospace and medical industry to build complex parts directly from computer-aided design. Due to the presence of large temperature gradients and rapid cooling rates during the processing, the PBF process is assumed to follow a rapid solidification processing route. However, the extent of deviation of the solid-liquid interface from equilibrium as a function of processing conditions has not been studied in detail for the PBF process. In this thesis, a numerical model is developed to study the interfacial characteristics as a function of processing conditions to characterize if the PBF process exhibits rapid solidification or not. The model is based on the work of Hunt et al. [1, 2, 3] and is capable of simulating cellular and dendritic growth at both low and high interface velocities. The developed model accounts for the various undercooling such as constitutional and curvature undercooling, the variation of the liquidus temperature with composition, and the partition coefficient and diffusion coefficient with temperature. Moreover, the variation of the partition coefficient and the liquidus slope with the growth velocity has also been considered in the developed model. The model is used to predict the range of primary cellular/dendritic spacing for a given set of input parameters. In addition to this, the tip undercooling, tip Péclet number and spacing Péclet numbers have also been estimated using the

model to quantify the extent of deviation of the solid-liquid interface from equilibrium. A good qualitative agreement between the predicted values from the numerical model and the analytical KGT model is achieved. This new model can be used to understand the relationship between the processing conditions, material system and interfacial characteristics during the PBF process, and thus improve microstructural development during PBF processing.

The thesis is dedicated to my beloved parents, sisters and my late dear friend Vaibhav Kiran Patidar for all their love and support.

Acknowledgements

I would like to express my sincere gratitude to several people who supported me throughout this journey. First and foremost, I'd like to thank my supervisor Prof. André Phillion for his guidance, encouragement and endless support. Next, I will like to thank Prof. Bartek Protas, Department of Mathematics, McMaster University for his insightful and constructive feedback on the numerical model. My gratitude also goes to my committee member Dr. Greenwood for providing me with good suggestions during my master's journey. Additionally, I will also like to thank my colleagues at SIM3P, especially Pardis Mohammadpour, Zhen Li, Angshuman Podder and Yi Feng for their support, encouragement and productive discussions. Last but by no means least, I would like to thank my parents and sisters for their unconditional love and support.

Contents

List of Figures

List of Tables

Notation, Definitions, and Abbreviations

Notation

A_e	Area of east control volume surface
A_w	Area of west control volume surface
A_n	Area of north control volume surface
A_s	Area of south control volume surface
A_i	Area of interfacial control volume surface
C_0	Initial/Bulk liquid composition
C_l	Composition in the liquid phase
C_s^*, C_l^*	Solute concentration in the solid and liquid phases of a binary alloy at the solid/liquid interface
C_l^e	Equilibrium liquidus composition

C_l^i	Kinetic liquidus composition
C_t	Tip composition
c	Volumetric specific heat
d_0	Capillary length
D_i	Interface diffusion coefficient
D_l	Solute diffusivity in the liquid phase
D_0	Diffusivity constant
E_1	Exponential integral function
G	Thermal gradient
G_m	Mean thermal gradient
G_s, G_l	Thermal gradient in the solid and the liquid phase respectively
G_c	Solute gradient in the liquid phase
g_l	Liquid volume fraction in the cell at a distance z behind the tip
$J(x)$	Jacobian Matrix
k	Partition coefficient
k_e	Equilibrium partition coefficient
k_v	Velocity dependent partition coefficient
K_s, K_l	Thermal conductivity of the solid and the liquid phase respectively

K_1, K_2	Principal curvatures of a surface
l_D	Solute diffusion length
l_T	Thermal diffusion length
L_1	Length of the cell behind the tip
L_2	Length of the cell ahead of the tip
m	Liquidus slope
m_v	Velocity dependent liquidus slope
$\mathbf{p}$	Direction vector
P_i	Interface Péclet number
P_t	Thermal Péclet number
P_c	Solutal Péclet number
Q	Activation energy
R_g	Gas constant
R	Dendritic tip radius
R_c	Critical tip radius
T	Temperature
T_L	Liquidus temperature
T_S	Solidus temperature

T_f	Melting point of a pure substance
T_f^{∞}	Equilibrium melting temperature with a planar interface
T_f^r	Equilibrium melting temperature with a curved interface
T^*	Interface temperature
T_0	Maximum interface temperature for partitionless solidification
v_m	Molar volume
V	Solid-liquid interface velocity
V_n	Solid-liquid interface normal velocity
V_0	Maximum crystallization velocity (∼Velocity of sound)
V_a	Critical growth rate for absolute stability
V_c	Critical growth rate for constitutional undercooling
W	Cell width/radius
x^c	Distance in the computational domain
$\mathbf{x}$	Solution vector
α_s, α_l	Thermal diffusivity in the solid and the liquid phase respectively
β	Factor controlling the distribution of grid points in the physical domain
Γ	Gibbs-Thomson coefficient

θ	Angle between the interface surface normal and the crystal axis
κ	Mean curvature
μ_k	Kinetic coefficient
δ	Positive scalar value
δ_i	Inter-atomic distance (Diffuse interface width)
∇^2	Laplacian operator
ΔH_f	Latent heat of fusion per mole
ΔT	Undercooling
ΔT^0	Unit undercooling ($\Delta H_f / v_m c$)
Δ	Dimensionless undercooling ($\Delta T / \Delta T^0$)
ΔT_k	Kinetic undercooling
ΔT_0	Liquidus-Solidus range at C_0
ΔT_0^v	Velocity dependent Liquidus-Solidus range
ΔS_f	Entropy of fusion per mole
λ	Cell spacing
λ_1	Primary spacing dendritic structures
λ_2	Secondary spacing dendritic structures
λ_e	Interphase spacing for eutectics

Ω	Dimensionless solutal supersaturation
σ^*	Stability constant
ξ_i	Péclet number dependent function
ϵ	Surface energy anisotropy parameter
ζ	Anisotropy function
$\hat{n}$	Unit interface normal vector
$\Gamma_1, ..., \Gamma_5$	Domain Boundaries

Abbreviations

AM	Additive Manufacturing
MAM	Metal Additive Manufacturing
PBF	Powder Bed Fusion
PBF-L	Powder Bed Fusion Laser
PBF-EB	Powder Bed Fusion Electron Beam
DED	Direct Energy Deposition
EB	Electron Beam
MSC	Marginal Stability Criteria
IMS	Ivantsov-Marginal Stability

RS	Rapid Solidification
MD	Molecular Dynamics
MC	Monte Carlo
PFC	Phase Field Crystal
PF	Phase Field
FT	Front Tracking
VOF	Volume of Fluid
LSM	Level Set Method
EM	Enthalpy Method
PFT	Pseudo Front Tracking
CA	Cellular Automata
m-CA	Modified Cellular Automata
DNN	Dendritic Needle Network
CAFE	Cellular Automata coupled with Finite Element
m-CAFE	Modified Cellular Automata coupled with Finite Element
CET	Columnar to Equiaxed Transition
SMS	Solidification Microstructure Selection
CV	Control Volume

PETSc Portable, Extensible Toolkit for Scientific Computation

Chapter 1

Introduction

This chapter provides an overview of Additive Manufacturing (AM) technology with an emphasis on the Metal Additive Manufacturing (MAM) process. This is followed by an introduction to the industrially relevant MAM processes of Powder Bed Fusion (PBF) and Direct Energy Deposition (DED) along with a discussion of the significant challenges inherent to MAM processing. In addition to this, the relationship between the underlying physical processes, microstructure, properties and defect formation during the MAM process is also briefly reviewed.

1.1 Additive Manufacturing

In the Additive Manufacturing process, also referred to as 3D printing or rapid prototyping, a component is built in a layer by layer manner by progressively adding material one layer at a time until the part is complete [10, 11, 12, 13]. It is different from the conventional manufacturing processes, sometimes referred to as subtractive

manufacturing, wherein a part is made by removing excess material from the feedstock or sheet metal [14, 11]. AM started as a technology for rapid prototyping in the 1980s. It was initially limited to only printing polymeric and porous substances [11]. However since its inception, the AM technology has grown tremendously and can now be used to print metals, ceramics, biomaterials and composites [15].

In recent years, the interest in AM has grown tremendously due to its inherent advantage over the conventional manufacturing process. AM offers freedom of design due to its ability to build complex geometries directly from computer-aided design without any need for costly tooling or forms. The manufacturing freedom in the AM process has caught the eyes of the aerospace, biomedical, energy, automotive industry along with hobbyists and artists alike [10, 11]. In contrast to the conventional manufacturing process, the flexibility offered by AM allows for the design of highly optimized functional/structural components by realizing complex hollow structures, overhangs and lattice structures. Furthermore, leaner part designs can lead to a reduction in total part counts by reducing or eliminating part assembly [14, 16]. AM is an economically viable route for producing highly customized parts in low volume and is well suited for low-to-medium volume productions [10].

AM began as a rapid-prototyping process, however owing to the advances in the technology, reduction in the cost of production, and improvement in part-density and part-quality, AM has evolved into an important manufacturing process in its own right. Nowadays, it is possible to print high-quality structural and functional parts that meet the accepted quality requirements of a certified production. Still, the widespread adoption of AM is plagued by the large variability in the quality/properties of the parts produced [11, 10].

Numerous AM technologies for printing metals have been developed over the past years. These technologies can be classified based on the feedstock such as powder, wire or sheets or the process used to consolidate the feedstock into a dense part. The parts are consolidated either by melting the feedstock using a heat source followed by subsequent solidification or by the use of ultrasonic vibrations. The ASTM F42 Committee has classified MAM into four categories [10, 11, 13]:

1. Powder Bed Fusion (PBF).
2. Direct Energy Deposition (DED).
3. Binder Jetting.
4. Sheet Lamination.

Among the technology available for printing alloys, the Powder Bed Fusion and Direct Energy Deposition processes are of the utmost importance to industry [11]. In both PBF and DED, the underlying process is similar wherein the feedstock is melted locally by the use of a high energy density heat source which on subsequent cooling results in the microstructure development [10]. A brief discussion of the two processes is given below.

1.2 Powder Bed Fusion

In the PBF process, a part is built selectively and locally by melting a thin layer of powders particles using either a laser (PBF-L) or an electron beam (PBF-EB) as the heat source. On subsequent cooling, this new layer forms a part of the build. This process is repeated in a layer by layer manner until the component is complete. In

the present work, the term PBF has been used to refer to both the laser and electron-beam based PBF process, whereas, the PBF-L and PBF-EB are used when specifically talking about one of the aforementioned processes. A schematic of a PBF-L setup is shown in Figure 1.1. Although both systems use the same powder-bed principle, there are some key differences in the hardware setup of the two [10, 11, 13]. PBF-L takes place in an inert environment, whereas PBF-EB takes place in a vacuum chamber and applies only to electrically conducting materials. Additionally, PBF-EB is a two-step process. In the first step, the powder particles are lightly sintered using the diffused electron beam to prevent electrostatic charging and repulsion of the particles. In the second step, the electron beam is used to fuse the particles to the previous layer.

PBF is increasingly used in the aerospace and biomedical industries to build components with complex designs. Although the build volume is small compared to other MAM techniques, the method offers increased versatility to manufacture various free-form structures with complex internal geometries. The PBF process also provides better dimensional tolerance and surface finish in comparison to other AM processes [17].

1.3 Direct Energy Deposition

Unlike the PBF process, in the DED process, the feedstock is ejected through a nozzle which is melted using a heat source and deposited in the desired location. The feedstock can be either metal powder or metal wires. The commonly used heat source is either a laser or an electron beam. Apart from these, plasma arc and gas metal arc can also be used as a heat source in the DED process [11, 10, 13]. Figure 1.2 shows a schematic of a powder fed and wire fed DED system with a laser and an electron

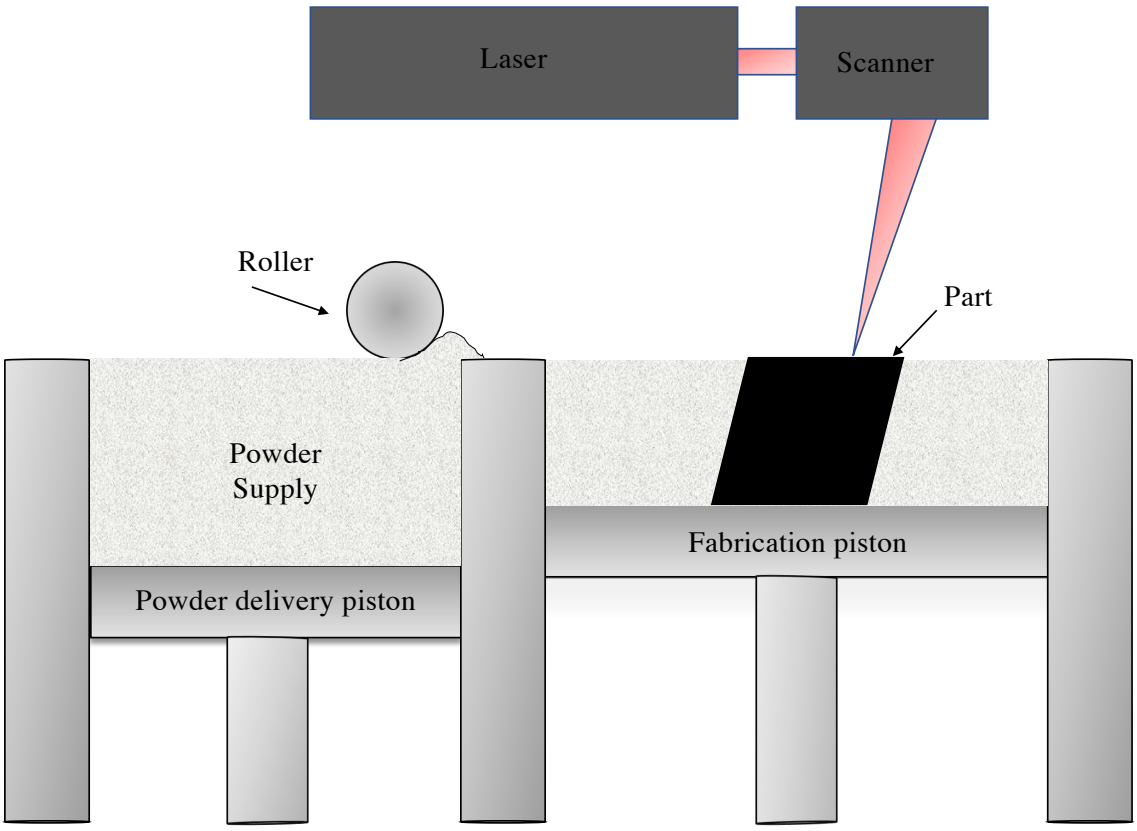

Figure 1.1: Schematic of a laser powder bed fusion (PBF-L) setup.

beam heat source. For non-reactive metals, the molten melt pool is protected from oxidation by the use of a shielding gas such as argon or helium. In the case of powder-fed DED, the shielding gas also helps to carry the powder particles to the melt pool. Whereas for reactive metals, the build chamber is filled with an inert gas [10, 13]. The build volume in the case of DED is large in comparison to the PBF process. However, the dimensional tolerance and surface finish is not as good as the PBF process. In addition to this, the DED process is also used for repairing components, therefore, making it an important MAM technology [17, 10, 13].

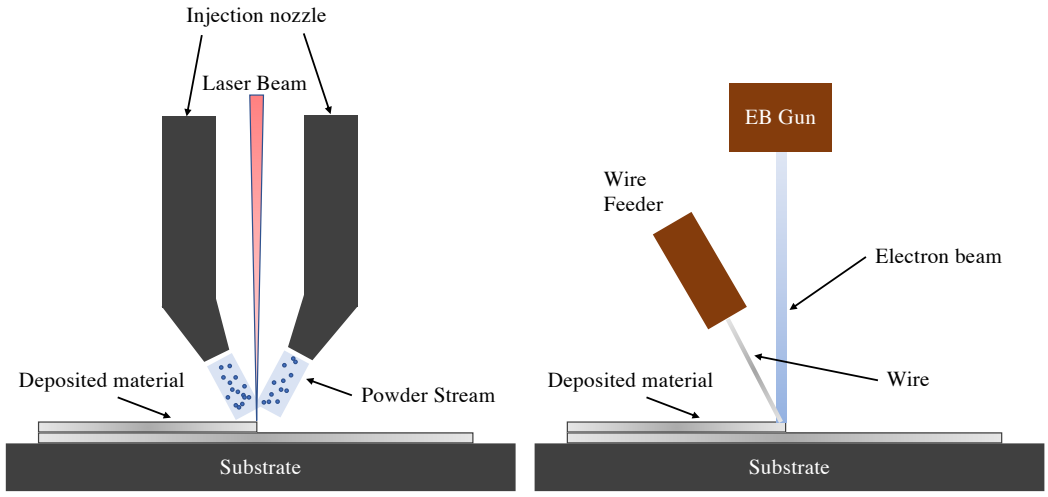

Figure 1.2: Schematic of (a) powder fed (laser) and (b) wire fed (EB) DED system.

1.4 Challenges: Metal Additive Manufacturing

As in any manufacturing process, the main challenge in MAM is the reliable production of high-quality defect-free parts. Defects such as porosity, lack of fusion, cracking, delamination, loss of alloying elements, anisotropic material properties and residual stresses are among the main processing challenges associated with the MAM. The quality and the properties of a part produced by MAM is affected by the process (PBF/DED), process parameters, scan strategy, feedstock quality, build chamber atmosphere and many other parameters [13, 10, 18, 19]. Understanding the relationship between the underlying physical phenomena, feedstock material, and processing route on the material properties of the components and defect distribution is crucial for the widespread adoption of the technology.

The physical properties of a metallic part depend upon the underlying microstructure and the defects [4]. These, in turn, are influenced by the solidification kinetics.

In the MAM process, the solidification kinetics depends upon the characteristics of the melt pool and the subjected thermal cycle. Whereas, the shape, size and temperature profile of the melt pool depends on the interaction of the heat source (power, speed and size) with the feedstock. After the initial solidification, the thermal cycling and cooling further influence the phase, grain growth and precipitation kinetics during the MAM process [13].

Melt pool characteristics also affect defect formation during the MAM process. Loss of alloying elements takes place when the melt pool temperature is too high, resulting in compositional changes affecting the solidification microstructure, corrosion resistance and mechanical properties of the component. Unduly high energy density can result in keyhole formations in a component, which can destabilize and collapse, resulting in voids and porosities. In contrast, the lack of fusion can result from inadequate power supply [10, 13].

As described above, the same set of process parameters that affect the MAM melt pool formation and temperature distribution not only influence the microstructure formation and subsequent growth kinetics but also affects the defect formation. Therefore, it is of utmost importance to study the relationship between the process parameters, microstructure and defect formation to identify the optimum processing conditions which not only result in the desired microstructure but also reduce the manufacturing defects within the parts.

1.5 Outline

This thesis proposes the use of numerical modelling and simulation to study the solidification characteristics during the metal additive manufacturing process. A computational model is used to predict the interfacial characteristics during the PBF-L process to establish the relationship between the processing and interfacial conditions. The model is applied to laser resolidified Al-Cu alloy and the results are compared with analytical growth theories.

This thesis is organized in the following order:

Chapter 2 describes the fundamentals of the solidification process as well as some details of methodologies to numerically model solidification microstructure evolution;

Chapter 3 presents the scope and objective of this work;

Chapter 4 describes in detail the numerical model used in this study;

Chapter 5 reports the application of the model applied to binary Al-Cu alloy and the corresponding results; and

Chapter 6 summarizes the key results of this work, limitations of the developed model and suggestions for future work.

Chapter 2

Literature Review

Solidification is a phase transformation process wherein a liquid turns into a solid. It is an important industrial technique that underpins most of the manufacturing processes. Solidification of a metallic melt involves a complex interplay of many physical processes occurring at different length scales and results in the formation of crystals. Depending upon the processing conditions, the crystal structures formed can exist in different phases and exhibit a wide range of microstructures. These phases and microstructure depend upon the thermodynamics and kinetics of the solidification process [4, 20, 21]. In what follows, the thermodynamics and kinetics of the solidification processing are discussed in detail, along with the discussion of relevant MAM microstructures. Finally, we will look at different approaches to numerically model and simulate the solidification process.

2.1 Solidification Processing

The process of solidification begins with the extraction of heat from the melt. The extraction of the heat results in a decrease in the enthalpy of the solid and the liquid phase. There is a further decrease in the enthalpy during the phase transformation from the liquid to the solid phase equal to the latent heat of fusion ΔH_f [22, 23].

In pure metals, the temperature at which phase transformation takes place is uniquely defined and is known as the melting point T_f of the substance. The melting point of a pure substance is used to sharply define an interface between the solid and the liquid phase. In the case of alloys, however, the phase transformation takes place over a range of temperatures and the interface between the solid and the liquid phase is given by a region of finite thickness known as the mushy zone [22, 23, 21].

In practice, the solidification of pure metals is seldom encountered. Even the commercially pure metals have enough impurities to change the solidification characteristics to that of an alloy [24]. Phase diagrams are useful in predicting the solidification path, the phases present and their composition in equilibrium. A hypothetical binary alloy phase diagram with an alloy of composition C_0 maintained at the temperature T^* and growing with a plane front is shown in Figure 2.1.

In considering alloy solidification it is further useful to define the partition coefficient k as

$$k = \frac{C_s^*}{C_l^*}, \tag{2.1.1}$$

where C_s^* and C_l^* are the composition of the solid and the liquid phase at a given temperature.

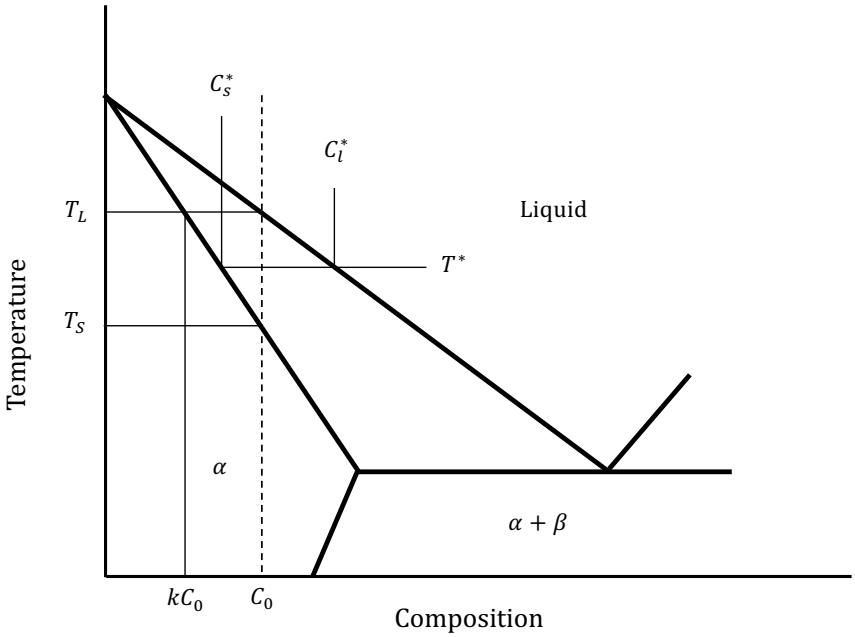

Figure 2.1: A hypothetical binary alloy phase diagram with linear solidus and liquidus line.

The equilibrium condition requires that there be no gradients in temperature nor in phase composition. Furthermore, the composition of the solid and the liquid at a given temperature T^* i.e. C_s^* and C_l^* respectively, are fixed by the phase diagram. However, in practice, the solidification process is never slow enough to meet the conditions for the equilibrium solidification [25].

The presence of thermal and compositional gradients causes deviation from the equilibrium. Furthermore, at equilibrium solidification cannot proceed since the rate of atom attachment at the solid-liquid interface will be equal to the rate of atom detachment. For solidification to proceed, some degree of deviation from the equilibrium is required at the solid-liquid interface to act as the phase change driving force. The presence of curvature or surface energy, the kinetics of attachment at the solid-liquid interface and solute trapping can cause further deviation from the equilibrium

conditions.

In practice, the solidification process can be classified in a well-defined hierarchy depending upon the degree of departure from the equilibrium as shown in Table 2.1. The extent of deviation of the interface from the equilibrium is directly correlated with the rate of advancement of the interface (interface velocity) or the extent of driving force for the solidification (amount of undercooling).

Table 2.1: Hierarchy of Equilibrium [8]

1. Full Diffusional (Global) Equilibrium
   (a) There are no chemical potential gradients (compositions of phases are uniform).
   (b) There are no temperature gradients.
   (c) The Lever rule is applicable.
2. Local Interfacial Equilibrium
   (a) The chemical potential is continuous across the interface.
   (b) The phase diagram gives compositions and temperatures only at liquid-solid interface.
   (c) Corrections must be made for interface curvature (Gibbs-Thomson effect).
3. Metastable Local Interface Equilibrium
   (a) Is important when stable phases cannot nucleate or grow sufficiently rapidly.
   (b) The interface condition is given by a metastable phase diagram, i.e. a true thermodynamic phase diagram that is missing the stable phase or phases.
4. Interfacial Non-equilibrium
   (a) The phase diagram fails to give temperature and composition at interface.
   (b) The chemical potentials are not equal at interface.

2.1.1 Local Interfacial Equilibrium

In practice, thermal and compositional gradients exist within the phases during solidification. However, if the rate of diffusion of the atoms across the interface is fast enough in comparison to the rate of the advancement of the interface V, the gradient across the interface will equilibrate much more quickly than in the bulk phase and the condition of local interfacial equilibrium can be assumed. Under these conditions, the conservation equations for the diffusion of temperature and mass within the phases along with the temperature and compositions at the interface given by the phase diagram define the kinetics of solidification [8].

As mentioned previously, the departure from the equilibrium also occurs due to the presence of boundary curvatures, therefore, the capillary effect needs to be incorporated to determine the shift in the equilibrium when the interface is not planar. The shift in the freezing point is given by the Gibbs-Thomson equation [21]

$$T_f^r = T_f^\infty - 2\Gamma\kappa, \tag{2.1.2}$$

where T_f^∞ and T_f^r is the equilibrium melting temperature of a planar and curved interface respectively, Γ is the Gibbs-Thomson coefficient and κ is the mean curvature.

If the solid-liquid interface is in motion, the interface attachment kinetics can lead to further deviations from the equilibrium. The relationship between the interfacial normal velocity and the kinetic undercooling is often expressed as [21]

$$V_n = \mu_k \Delta T_k, \tag{2.1.3}$$

where μ_k is the kinetic coefficient and ΔT_k is the kinetic undercooling. For most

metals at low solidification velocities, the undercooling required is very small and the actual interface velocity can be calculated from the bulk diffusion considerations only. However, kinetic effects cannot be neglected at high growth velocities i.e., under interfacial non-equilibrium conditions.

2.1.2 Metastable Equilibrium

Metastable equilibrium is important in many metallurgical processes. When the free energy is minimum but not absolute minimum, metastable equilibrium occurs. This is often the case when large fluctuation (nucleation) is necessary for the growth of a stable phase. Metastable transformation takes place at high growth velocities when many stable phases with complex crystal structures have difficulty in nucleation and growth. Under the conditions of metastable equilibrium, the solid-liquid interface can still be assumed to be in local equilibrium [8].

2.1.3 Interfacial Non-Equilibrium

When the rate of advancement of the solid-liquid interface V is comparable to the rate of diffusion of the solute atoms across the solid-liquid interface, there will not be enough time for the compositions to equilibrate near the interface and the assumption of local interfacial equilibrium will not hold true [4]. Significant non-equilibrium effects such as the formation of metastable phases, increased solute solubility at levels exceeding the equilibrium solubility in the solids and novel microstructures have been experimentally observed at high growth rates. Highly undercooled melt or a fast-moving temperature field can result in the rapid growth of the solid phase [8, 4].

The rate of diffusion of the solute atoms across the interface is given by the inter-atomic diffusion rate D_i/δ_i, where D_i is the interfacial diffusion coefficient and δ_i is the inter-atomic distance (width of the diffuse interface). When the rate of interface advancement is very rapid ($V_n >> D_i/\delta_i$), the crystal will not have enough time to rearrange its composition and all the solute atoms will be trapped inside the solid. This phenomenon is referred to as partitionless solidification. Partitionless solidification takes place when the interface temperature is significantly below the liquidus temperature T_L. The maximum temperature at which the partitionless solidification can take place is restricted by the thermodynamic considerations and is called the T_0 temperature. At the T_0 temperature, the molar free energy of the solid and liquid phase is equal for a given composition.

Under the conditions of interfacial non-equilibrium, the phase equilibria need to be appropriately modified to express the variation in the interface temperature and solid composition that are produced at high-velocity as [4]

$$T^* = T(V, C_l^*) - 2\Gamma\kappa, \tag{2.1.4}$$

$$C_s^* = C_l^* k(V, C_l^*), \tag{2.1.5}$$

where $T(V, C_l^*)$ and $k(V, C_l^*)$ represents the changes in the equilibrium freezing temperature and partition coefficient at high velocities. The functions $T(0, C_l^*)$ and $k(0, C_l^*)$ are equal to the equilibrium values given by the phase diagram when the interface velocity is zero [4].

Several models have been proposed in the literature to model the dependence of

partition coefficient with velocity. One of the simplest and most widely accepted model which agrees well with the experiments was proposed by Aziz [26]. The model ignores the dependence of the partition coefficient with composition and is expressed as

$$k_v = \frac{k_e + \delta_i V/D_i}{1 + \delta_i V/D_i}, \tag{2.1.6}$$

where k_e is the equilibrium partition coefficient and the parameter $\delta_i V/D_i$ can be regarded as the interface Péclet number P_i. Figure 2.2 shows the variation of the partition coefficient with velocity.

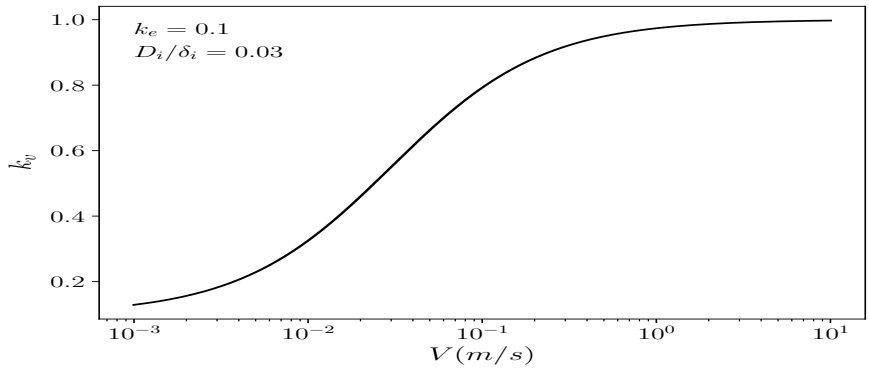

Figure 2.2: Variation of the partition coefficient with the growth velocity [4].

As $k_v \to 1$, the second condition that needs to be satisfied is $T^* \leq T_0$. Neglecting the curvature effect, the interface temperature for a flat interface with kinetic undercooling can be written as [4]

$$T^* = T_f^\infty + m_v C_l^* - \frac{R_g T_f^\infty}{\Delta S_f} \frac{V}{V_0}, \tag{2.1.7}$$

where R_g is the gas constant, ΔS_f the entropy of fusion, V_0 the collision limit of atom

attachment i.e., the maximum velocity at which the atoms can still attach to the crystal (its upper limit is speed of sound in metals), and m_v is the apparent liquidus slope at high velocities and is expressed as

$$m_v = m \left[1 + \frac{k_e - k_v \left[1 - ln(k_v/k_e) \right]}{1 - k_e} \right], \tag{2.1.8}$$

2.1.4 Solidification in Metal Additive Manufacturing

In the MAM process, the consolidation of the metal powder happens by a fast-moving laser or electron beam heat source resulting in the local melting of the metal powders. The local melting of powder particles is followed by subsequent cooling and solidification. The MAM process is characterized by high thermal gradients and rapid cooling, which during solidification, can lead to the deviation from the local interfacial equilibrium. The actual temperature field in the fabricated part has a complex temporal distribution and each layer experiences multiple re-heating and re-cooling cycles. Furthermore, the process parameters including energy density, layer thickness, surrounding material and pre-heat temperature greatly affect the temperature gradient in the melt pool [11, 17, 10].

Experimental measurements of the temperature field during the MAM process is not straightforward due to the highly transient distribution. Several experimental techniques such as placing thermocouples at monitoring locations in the melt pool, infrared imaging and in-situ x-ray synchrotron measurements have been used to measure relevant temperature distribution, thermal gradients and cooling rate [27, 28, 29, 30, 31, 32]. However, it is difficult to measure the temperature distribution in the melt pool accurately with thermocouples and infrared imaging can only provide

the surface temperature distribution and not the bulk 3D profile. An alternative approach to predict the temperature distribution and the cooling rate in the melt pool is through the use of computational models. Computational models can provide the knowledge of the transient 3D temperature distribution, however, 3D transient heat transfer analysis during MAM is a challenging task due to complex physical processes involved [10, 33, 19, 34]. The typical thermal gradient and cooling rate measured during the MAM process is reported in Table 2.2.

Table 2.2: Typical thermal gradients and cooling rate during MAM.

Process	Thermal gradient (K/m)	Cooling rate (K/s)	
PBF-L	$\mathcal{O}(10^6 - 10^7)$	$\mathcal{O}(10^3 - 10^8)$	[35, 30, 31]
PBF-EB	$\mathcal{O}(10^5)$	$\mathcal{O}(10^3 - 10^4)$	[36]
DED	$\mathcal{O}(10^3 - 10^5)$	$\mathcal{O}(10^2 - 10^3)$	[37, 38, 28]

In MAM, most of the heat is extracted through the substrate which acts as the heat sink. As the component increases in height, the heat conduction through the substrate decreases resulting in increased melt pool size and peak temperatures in the melt pool. The local thermal gradients and cooling rates also vary greatly depending upon the alloy system, processing condition, as well as location within the melt pool. Moreover, as the distance between the layers and the substrate increases, the cooling rate is expected to decrease. The most important parameters that affect the solidification structure are the local solidification growth rate, V, and thermal gradient, G [10]. Figure 2.3 shows the relationship between the MAM processing parameters and the solidification microstructure, linked through the melt pool formation.

As seen in Figure 2.3, the ratio G/V affects the solidification morphology whereas

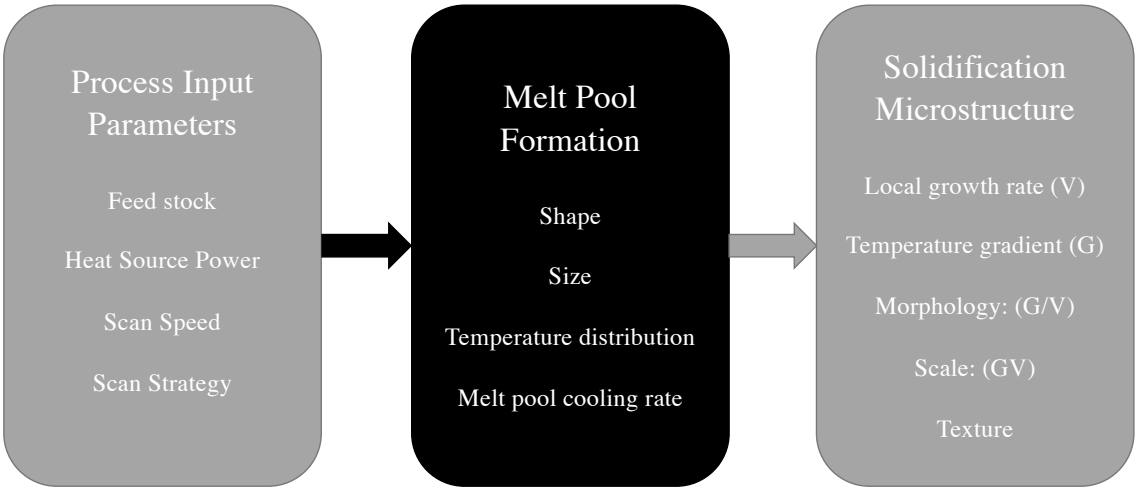

Figure 2.3: Relationship between the MAM processing parameters and the solidification microstructure through the melt pool formation.

the cooling rate $G \cdot V$ affects the size of these structures. The variations in the cooling rate and thermal gradient at different locations during the built results in the inhomogeneity in the microstructure and the physical properties of the parts produced by MAM. Moreover, the microstructure and the grain structure at different locations are further modified due to repeated heating and cooling cycle as the build progresses [10]. Therefore, to characterize the microstructure and predict the properties of the parts built using MAM, it is essential to understand the evolution of the microstructure with the processing conditions and as the build progresses in height during the manufacturing process. In what follows, the fundamentals of microstructure evolution is discussed in detail.

2.2 Solidification Microstructure

Solidification microstructures are the microscopic patterns that are observed in the $10\,\text{nm} - 100\,\mu\text{m}$ range when a liquid transforms to a solid [21]. According to Kurz, "A microstructure is defined by the entirety of phases, grains, defects and their respective morphologies, size, volume fractions, distributions, orientations, and crystallographic directions" [5]. Most of the commonly exhibited microstructures by a pure metal or an alloy can be classified into two categories: single-phase primary crystals (planar, cells or dendrites) and polyphase (eutectic) structures. These morphologies either develops as columnar (oriented) or equiaxed microstructures. Columnar microstructure develops when the heat flow is opposite to the growth direction (directional solidification) and is also known as constrained growth. In contrast, equiaxed microstructure grows when the heat flow and grain growth takes place in the same direction (undercooled melt) [4].

The solidification microstructure along with the defects in the crystal and the microsegregation profile largely controls the properties and the quality of the as-solidified component. Solidification microstructure also influences their behaviour in the subsequent forming processes [39, 40]. Thus microstructures act as a strategic link between material processing and material behaviour. Therefore it is of practical importance to study the relationship between the processing conditions and the microstructure that results in the desired properties in the parts.

Solidification microstructures are controlled by several processes taking place at different length scales. These processes depend upon the alloy composition, the material properties (liquidus slope, partition coefficient), thermophysical properties (diffusion coefficient, Gibbs-Thomson coefficient, thermal diffusivity) and also on the

processing conditions such as the applied thermal gradient, cooling rate which controls the flow of heat and mass through diffusion and convection [39, 40]. Over the past years, great progress has been made in understanding the relationship between the processing conditions and microstructure evolution through the development of analytical and numerical models and improved experimental techniques. In this work, the focus is on the single-phase primary crystals and in the subsequent sections, the theories of planar, cellular and dendritic growth are discussed in the detail. This is followed by the discussion of the microstructures observed during MAM processing.

2.2.1 Interface Dynamics

Solidification during MAM is characterized by the presence of a positive temperature gradient i.e., the heat flows from the melt to the solid. Under these conditions, the solid-liquid interface can exist in different morphologies depending upon the growth condition. A single-phase interface has been observed to go through the following sequence of interface morphologies: planar, cells, dendrites, cells, bands, planar as the growth rate increases [5]. The presence of constitutional undercooling at low velocities results in the destabilization of the interface. However, as the interface velocity increases, the non-equilibrium effects become important which leads to the re-stabilization of the interface as shown in Figure 2.4. The actual growth rates at which these transitions take place depends upon the temperature gradient at the interface, the alloy composition, and the interface attachment kinetics [39].

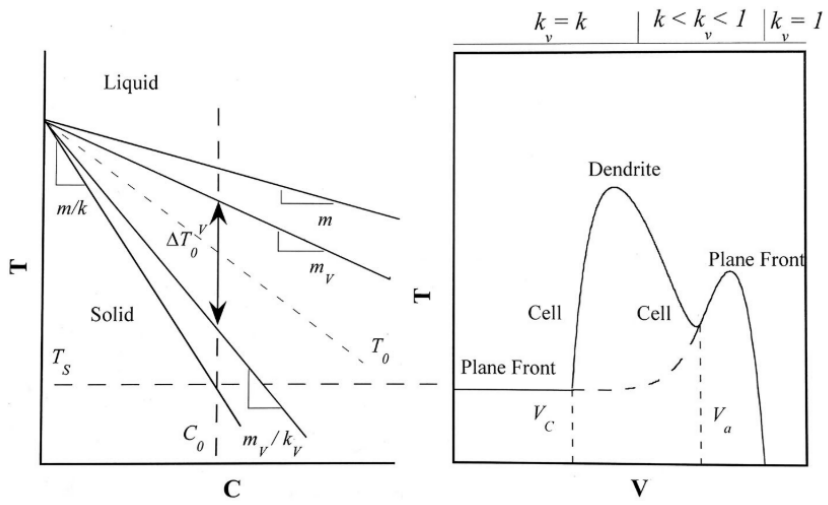

Figure 2.4: Solid-liquid interface temperature during directional solidification. (a) The equilibrium and non-equilibrium phase diagram. (b) Interface response as a function of growth velocity corresponding to the phase diagram. The continuous line in (b) corresponds to the approximate interface/tip temperature of the morphologically stable structure under steady state [5].

2.2.2 Planar Interface Growth

Planar interfacial growth is an important growth morphology since it results in the uniform composition in the solid during steady growth. The problem of interfacial stability has been studied by using the Mullins-Sekerka instability theory [41] and only for restricted growth velocities, the interface becomes unstable. However, most of the practical solidification conditions overlap with the instability region and therefore most of the solidification microstructures are dendritic [5]. The lower and the upper limit on the interfacial velocities is given by V_c (constitutional undercooling) and V_a (absolute stability) respectively i.e., for $V < V_c$ and $V > V_a$ the interface grows with planar morphology. The constitutional undercooling velocity is given as [5]

$$V_c = \frac{G_m D_l}{\Delta T_0}, \tag{2.2.1}$$

where D_l is the diffusivity coefficient in the liquid phase and $\Delta T_0 = T_L - T_S$ is the difference between the liquidus and solidus temperature at C_0. G_m is the mean thermal gradient at the interface and is given as:

$$G_m = \frac{G_s K_s + G_l K_l}{K_s + K_l},$$

where K_s and K_l are the thermal conductivities in the solid and liquid phase respectively. G_s and G_l are the thermal gradients in the solid and liquid phase respectively. The thermal gradients in the above equation are calculated at the interface. Finally, the velocity for the absolute stability is expressed as [5]

$$V_a = \frac{D_l \Delta T_0^v}{\Gamma k_v}, \tag{2.2.2}$$

and

$$\Delta T_0^v = \frac{C_0 m_v (k_v - 1)}{k_v},$$

where ΔT_0^v is the velocity-dependent temperature difference between the liquidus and solidus temperature for dilute solutions assuming linear phase diagrams.

2.2.3 Cellular Growth

During directional solidification, cellular growth takes place when the planar interface becomes unstable at low growth velocities or high velocities before the limit of absolute

stability. The cellular structures are characterized based on the cell tip composition or temperature, the spacing between the cell tips (periodicity of the cellular structure) and the interface shape near the grooves. Based on the experimental observations the cellular structures are classified into two types: low amplitude cells and large amplitude cells as shown in the Figure 2.5 [39].

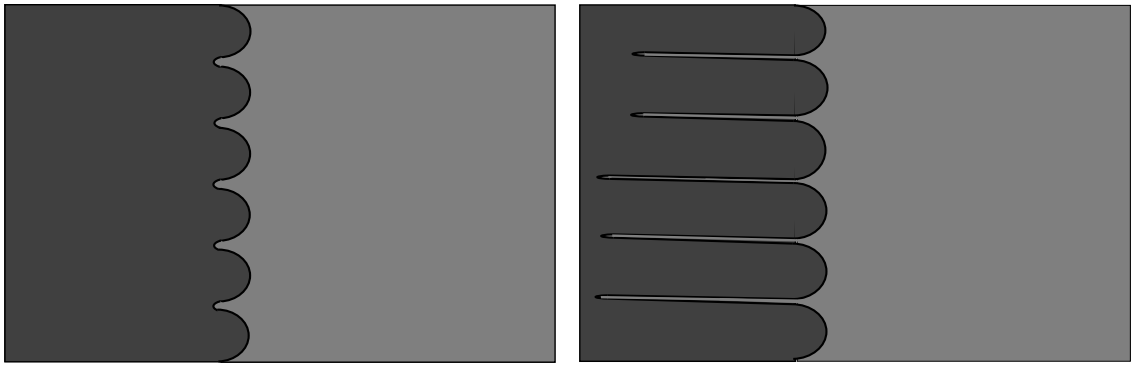

(a) Low amplitude cells (b) High amplitude cells

Figure 2.5: Growth morphologies of cellular structures.

Low amplitude interface cells forms at low and high velocities near the limit of planar interface growth. Significant differences in the concentration profile of low amplitude cells at low and high velocities have been found. Far from the threshold of planar stability large amplitude cells are formed [39].

The crucial role of crystalline anisotropy in influencing the cellular array stability has been shown using numerical and theoretical models [40, 42]. Moreover, the existence of a small range of stable spacing has also been studied using such models. In these studies, the cellular array was found to be unstable beyond a lower spacing limit with certain cells disappearing due to overgrowth. Above the critical upper spacing limit the tip-splitting was observed to take place [39, 2]. Furthermore, experimental studies on the transparent system have shown a selection of average cell spacing which

goes down with increasing velocity [43, 44, 45].

2.2.4 Dendritic Growth

Most of the solidification processing conditions lie in the region where the dendritic growth is stable and therefore dendritic structures are among the most prominent microstructures observed during solidification processing. It is also among the most complicated pattern formed during solidification and its ubiquity has made it one of the most studied microstructure during the grain growth process. The term 'dendrite' is derived from the Greek word for the tree (dendron) since the dendritic structures are highly branched with primary, secondary, tertiary and higher-order branches as shown in Figure 2.6 [46, 40, 39].

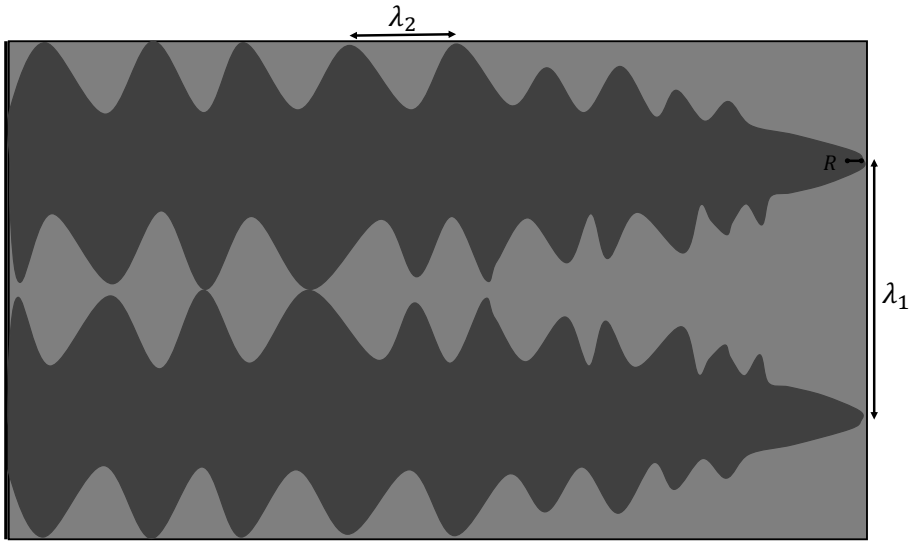

Figure 2.6: A schematic of a dendritic structure with the important length scales which are used to characterize the dendritic structures.

Several microstructural features such as dendritic tip radius R, primary spacing λ_1 (directional growth) and secondary spacing λ_2 are used to characterize the dendrites

as shown in Figure 2.6. Several theoretical and numerical models have been proposed in the literature to quantitatively model the relationship between the processing conditions and the characteristic length scales during dendritic growth. However, most of these models only consider an isolated dendritic tip. Nevertheless, these dendritic tip models have provided fundamental insight into the growth behaviour and help to determine the tip radius and tip composition as a function of growth velocity or the undercooling. Moreover, these models have been useful in predicting the microstructural transitions and creating microstructure selection maps [46].

Dendritic growth models

The first rigorous self-consistent model of a steady-state growth of an isolated thermal dendritic tip was proposed by Ivantsov. In the model formulation, Ivantsov made many simplifying assumptions such as the interface was assumed to be isothermal. Moreover, the curvature and interface kinetic effects were neglected. A relationship between the dimensionless undercooling and the thermal Péclet number was given by Ivantsov for the case of pure undercooled melt [39, 40, 46] and is expressed as

$$\Delta = P_t \exp(P_t) E_1(P_t), \tag{2.2.3}$$

where Δ is the non-dimensional undercooling and P_t is the thermal Péclet number defined as the ratio of dendritic tip radius R and thermal diffusion length $2\alpha_l/V$, with α_l being the thermal diffusivity in the liquid phase and E_1 the exponential integral function [40, 4]. Afterwards, Ivantsov extended his model to binary alloy dendrites and gave a relationship between the solutal supersaturation Ω, growth rate V and the tip radius R [4, 40] and is given as

$$\Omega = P_c \exp(P_c) E_1(P_c), \tag{2.2.4}$$

where the solutal supersaturation ($\Omega = \Delta C/\Delta C^*$) is given as the ratio of the change in the concentration of the tip ($\Delta C = C_t - C_0$), to the concentration difference at the tip ($\Delta C^* = C_t(1-k)$) and P_c is the solutal Péclet number, which is given as the ratio of the tip radius R, to the solutal diffusion length $2D_l/V$ [4]. Nonetheless, the solution of the Ivantsov equation did not give a unique solution for the dendritic growth. For a given undercooling or supersaturation the product of VR is constant and infinitely many solutions can exist.

The Ivantsov model neglected the capillary effects, consequently, neglecting the thermodynamic constraint on the critical tip radius R_c given by the critical radius of nucleation. At the critical radius, the supersaturation effect is counteracted by the curvature [4, 40]. So the next step was to include the capillary effect in the Ivantsov model. The modified Ivantsov model was proposed where the tip temperature/composition was modified by taking into account the capillary effects. Temkin further improved the Ivantsov model by accounting for the capillary and interface kinetic effects. The inclusion of the capillarity resulted in a maximum point in growth velocity. However, still, no unique solution was given by the modified theories, and at least one other phenomenon had to be considered [40, 39, 46]. Earlier, it was assumed that the dendrites select the tip radius which leads to the maximum growth rate (maximum-velocity principle), however, the results predicted by the maximum-velocity principle did not agree with the experiments [47, 48]. Interestingly, the shape of a actual dendrite is very similar to a paraboloid near the tip region, therefore the Ivantsov model was determined to be a reasonable solution for an isolated dendritic

growth [48, 40].

Marginal Stability Criteria

Langer and Müller-Krumbhaar performed a linear stability analysis of an Ivantsov paraboloid and found that of all the tip radius R, only a band of R gives a stable radius. They showed 'that dendrites that are too broad and slow growing suffer tip-splitting instabilities, whereas those which are too sharp and fast growing tend to broaden and slow down because of a side-branching instability' [49, 50]. Among the stable values of R, they found that the higher limiting value agreed remarkably well with the experiments done by Glicksman et al. [47, 48], leading to the proposal that the dendrite selects the largest stable radius and they called this criterion as 'marginal stability criteria'(MSC).

In the limit of low Péclet number the MSC predicts the relationship between the dendrite tip radius which has the form

$$R = \left[\frac{\Gamma/\sigma^*}{mG_c\xi_c - G_m}\right]^{1/2}, \tag{2.2.5}$$

where G_c is the solute concentration gradient, σ^* is a stability constant and ξ_c is a Péclet number dependent function [39]. Although, there is good agreement between the experimental results and the marginal stability criteria, however, it is not a rigorous criterion since there is no justification for the selection of one stable radius over all other stable values. Moreover, the model also ignores the effect of surface energy on the self-consistent growth model. With the addition of the capillary effect, the Ivantsov parabola does not remain shape-preserving. However, Langer and Müller-Krumbhaar assumed that the interface deviates only slightly from the steady-state

shape when isotropic capillary corrections are introduced.

Solvability Theory

The advent of MSC lead many authors to develop a mathematically rigorous model of self-consistent steady-state dendritic growth problem without any ad-hoc assumptions [51, 52, 53, 54, 55, 56]. From these studies, it was found that if isotropic capillarity or interface attachment is considered, no matter how small the effect, no steady-state dendrite solution exists. Only in the presence of anisotropic interfacial energy, a discrete set of steady-state shape shape-preserving solutions can be found [51, 52, 53, 54]. Out of these discrete sets of solutions, only the fastest one is stable against tip splitting instability [55, 56]. This stable solution gives a unique dendritic tip radius and is known as the microsolvability condition.

The solvability condition has been applied at low and high Péclet numbers to describe the relationship between the tip radius and growth velocity in both thermal and solutal dendritic growth problems [57, 58]. The relationship for the dendritic tip radius predicted by solvability condition is the same as equation (2.2.5) except the stability parameter is not a constant but rather depends on the surface energy anisotropy parameter ϵ.

The solvability condition shows that the steady-state dendritic shape is very close to a parabola therefore the solutal and thermal fields can be approximated from that given by the Ivantsov model [39, 46]. Although, the stability criteria predicted by MSC and solvability condition is generally viewed as $VR^2 =$ constant. However, this is only true for low Péclet number conditions. At high Péclet numbers i.e., greater than unity; VR^2 increases rapidly [59, 60].

2.2.5 KGT Model

In the 1980s, Kurz, Giovanola and Trivedi proposed an analytical model of direction solidification applicable under rapid solidification conditions by combining the Ivantsov solution with the marginal stability criteria. In the model, the radius of the dendritic tip is estimated using the critical wavelength of a marginally stable planar solid-liquid interface coupled with the solute trapping effect. In the KGT model, the relationship between the microstructural characteristics with the growth velocity is expressed as [60]

$$V^2 A + VB + C = 0, \tag{2.2.6}$$

with

$$\begin{aligned} A &= \frac{\pi^2 \Gamma}{P_c^2 D_l^2}, \\ B &= \frac{mC_0(1-k)\xi_c}{D_l[1-(1-k)Iv(P_c)]}, \\ C &= G, \end{aligned}$$

where $Iv(P_c) = P_c \exp(P_c) E_1(P_c)$ and ξ_c is given by the equation

$$\xi_c = 1 - \frac{2k}{[1+(2\pi/P_c)^2]^{1/2} - 1 + 2k}$$

The variation of the diffusion coefficient and the changes in the phase diagram with temperature have also been considered in the KGT model. The KGT model has been successfully applied to predict the experimental results and microstructure characteristics under rapid solidification conditions.

2.2.6 Rapid Solidification Microstructure

Rapid solidification (RS) processing often refers to solidification done under high cooling rates or high undercooling values. According to Kurz and Trivedi, "The best way to define RS is through the Péclet number of the corresponding microstructural feature: typically tip radius, R, for dendrites, cell spacing, λ, for cells, interphase spacing, λ_e, for eutectics, and atomic interface width, δ_i, for solute trapping" [39]. The classical growth theories based on low Péclet number approximation needs to be modified to account for the localization of the diffusion field under RS. Furthermore, the assumption of local interfacial equilibrium is no longer valid under RS.

Several authors have proposed theoretical models for predicting the microstructural features during rapid solidification. These models combine the transport model of Ivantsov with the marginal stability criteria including the solute trapping effects, the so-called IMS (Ivantsov-Marginal Stability) models [60, 61]. Good agreement between the experiments and the IMS theories has been found for a significant range of undercooling in many metals and alloys.

Very fine-grained microstructures have been observed at high growth rates for a large range of undercooling values. These fine-grained microstructures are believed to be the result of dendrite fragmentation. Fragmentation refers to the detachment of dendrite arms or trunks. These fragments can move into an undercooled melt and can initiate fine-grained equiaxed microstructures. Also, before the stabilization of the interface at high growth rates, very fine cellular structures are observed which are referred to as microcellular to differentiate them from the coarse cells [39, 40, 62].

Another interesting phenomenon that has been observed at high growth rates is the oscillatory behaviour of the solid-liquid interface known as banding. Banding

takes place in the regime between cellular-dendritic and planar front solidification where absolute stability is predicted by the absolute stability criteria. A banded microstructure is characterized by the presence of alternating planar front and cellular-dendritic structures which are approximately perpendicular to the growth direction. Periodicity of the bands has been observed to be independent of the growth velocity, whereas the fraction of the cellular-dendritic bands decreases with increasing growth rate [39, 46, 62].

2.2.7 Microstructure - Processing Relationship

Trivedi and Kurz showed that simple yet remarkable correlations exist between the physical process and the microstructural length scales. They did this by examining all the important physical processes that control the solidification microstructures i.e., thermal and solute diffusion, capillarity etc. and by associating a characteristic length scale to these physical phenomena. The basic conceptual approach behind this idea shown in the Figure 2.7 [6]. The characteristic length scale of the physical processes is listed in Table 2.3.

Table 2.3: Characteristic length scales of physical processes [6]

Characteristic Length	Undercooled Melt		Directional Solidification of alloys
	Pure	Alloy	
Solute diffusion length, l_D	D_l/V	D_l/V	D_l/V
Thermal length, l_T	α_l/V	α_l/V	$\Delta T_0/G$
Capillary length, d_0	$\Gamma/\Delta T^0$	$\Gamma/\Delta T_0$	$\Gamma/\Delta T_0$

Now, in a general alloy system where all three processes i.e., thermal, solute and

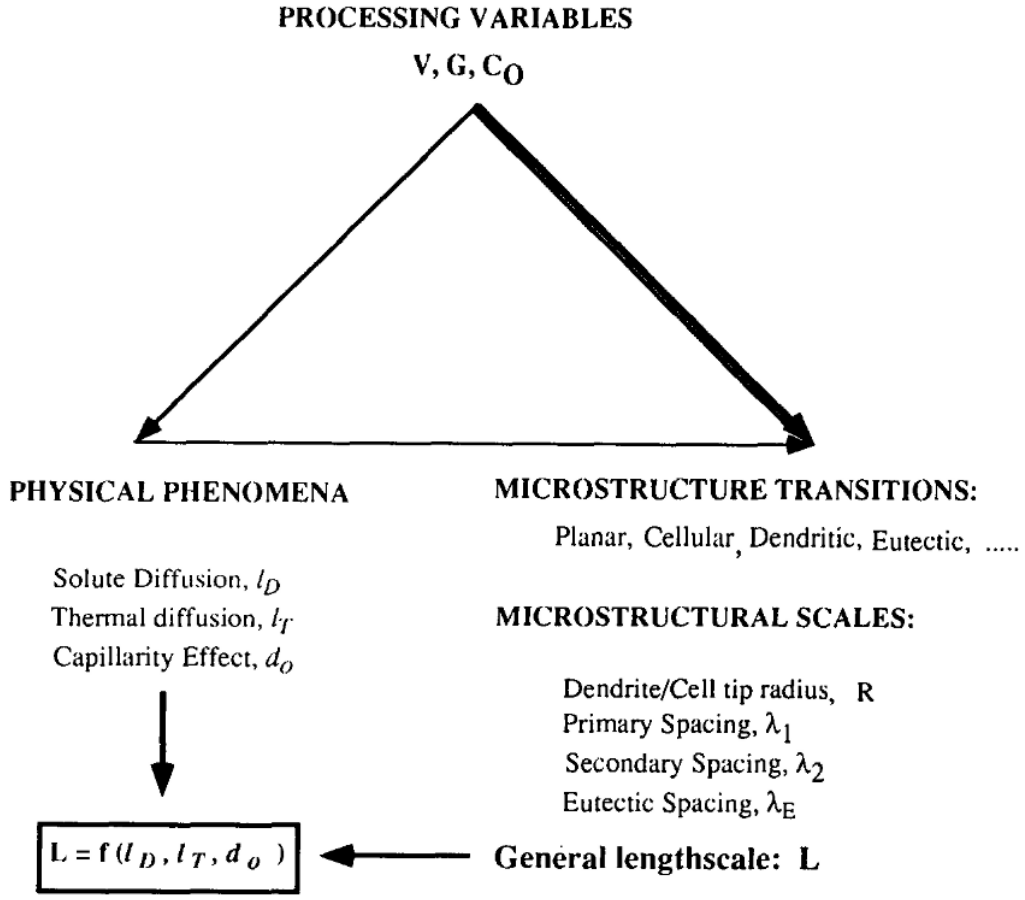

Figure 2.7: A basic conceptual approach relating the microstructural length scales with the physical processes through physical length scales [6].

capillary effects are important, the general microstructural length scale L_i can be given as [6]:

$$L_i = A[l_D]^a[l_T]^b[d_0]^c \tag{2.2.7}$$

where $L_i = (R, \lambda_1, \lambda_2, \lambda_e)$ is the characteristic length, the exponents a, b, c are constant whose sum must be equal to 1 and A is a constant of proportionality. Moreover,

the transition between different morphologies is the result of an interplay between different physical processes and this transition condition can be written in terms of the physical length scales. For directional solidification this is given as:

(i) Transition from planar to cellular growth at low velocity: $l_D = l_T$

(ii) Transition from the cell to dendrite at low velocity: $l_D = kl_T$

(iii) Transition from cellular to planar growth at high Velocity: $l_D = kd_0$

The transition from the dendrites to the cell at high velocities yet cannot be defined by this simple relation, however, it is believed to be of the form $l_D = \alpha d_0$, where α is some constant [6].

2.2.8 MAM Microstructure

During MAM, the feedstock material is subjected to complex heating and cooling cycles, hence many MAM processes can lead to the formation of meta-stable microstructure and non-equilibrium phase composition that can vary along the build height [11]. Fine columnar cellular-dendritic microstructures are among the most commonly observed structures during the MAM processing [63, 64, 65, 66, 67, 68]. These fine columnar microstructures are believed to be a result of high thermal gradients and rapid cooling rates. Although the above considerations are valid for all MAM processes, the exact phases and microstructure depend upon the alloy system and actual MAM processing route taken. In what follows the variables that control the microstructure formation during MAM are discussed in detail.

Solidification Selection Maps (SMS)

As mentioned previously, the thermal gradient G, and growth rate V are important parameters that affect the solidification microstructure and grain morphology that forms for a given alloy composition and processing conditions. SMS maps are an efficient tool that illustrates the structure-process relationship. They can be very helpful in effectively assessing the wide parameter space and can be helpful in the development of detailed numerical models [7].

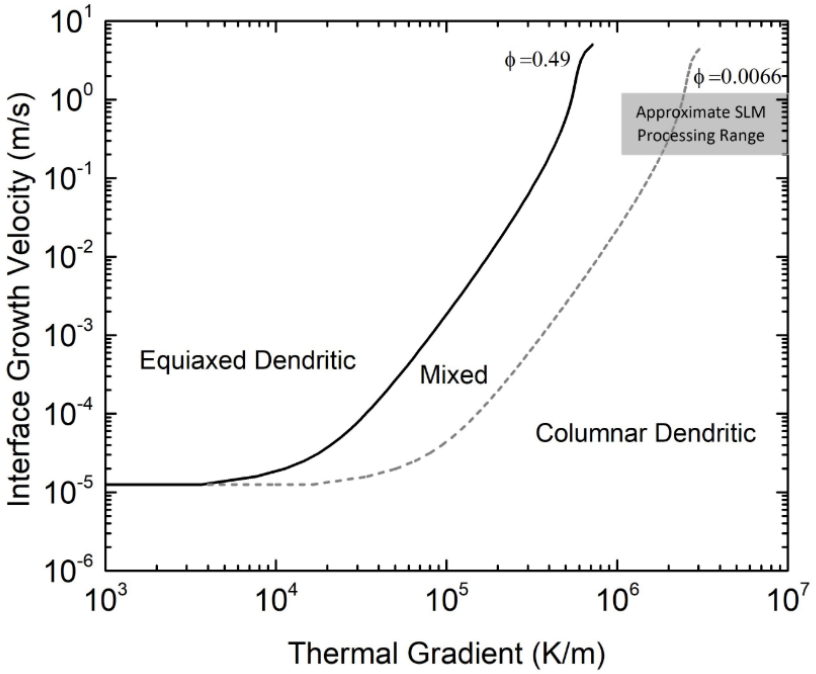

Figure 2.8: Type 2 SMS map for Al-10wt%.Si-0.5wt%.Mg alloy for PBF-L process [7].

Depending upon the value of the thermal gradient and growth rate, the solidification structure may undergo columnar to equiaxed (CET) transition as shown in the Figure 2.8. Using solidification maps one can figure out the values of G and V to get the desired microstructure.

Grain Structure

MAM alloys predominantly have oriented, columnar grains. The melt pool shape and size can significantly affect the grain structure in the MAM process. In the case of PBF systems which are characterized by fast scanning speeds, the grains are closely aligned with $\langle 100 \rangle$ build direction, whereas, in the case of DED, the grain orientation can significantly deviate from the build direction [10, 13].

2.3 Numerical Modelling

Quantitative prediction of solidification microstructure is a computational challenge owing to the multi-physics and multi-scale nature of the solidification phenomenon. Over the years, many computational models of the solidification and microstructure formation have been developed to study the various aspects of the multi-scale phenomenon, beginning with the nucleation and interfacial properties at the atomic scale to macro-scale heat and mass transfer [69, 70, 71]. Figure 2.9 list the different models that are used in the solidification study, these models have been roughly classified based on the physical length and time scales at which they are applicable.

All these models are important in the study of the solidification phenomenon and are linked with each other. The multi-scale approach involves calculating the desired properties at a given scale with inputs coming from the lower scale models and the outputs being used in the larger-scale models.

Atomistic simulations using Molecular Dynamics (MD) and Monte Carlo (MC) methods have been extensively used to study the interfacial properties such as the free-energy and the kinetic coefficient of the solid-liquid interface. These properties

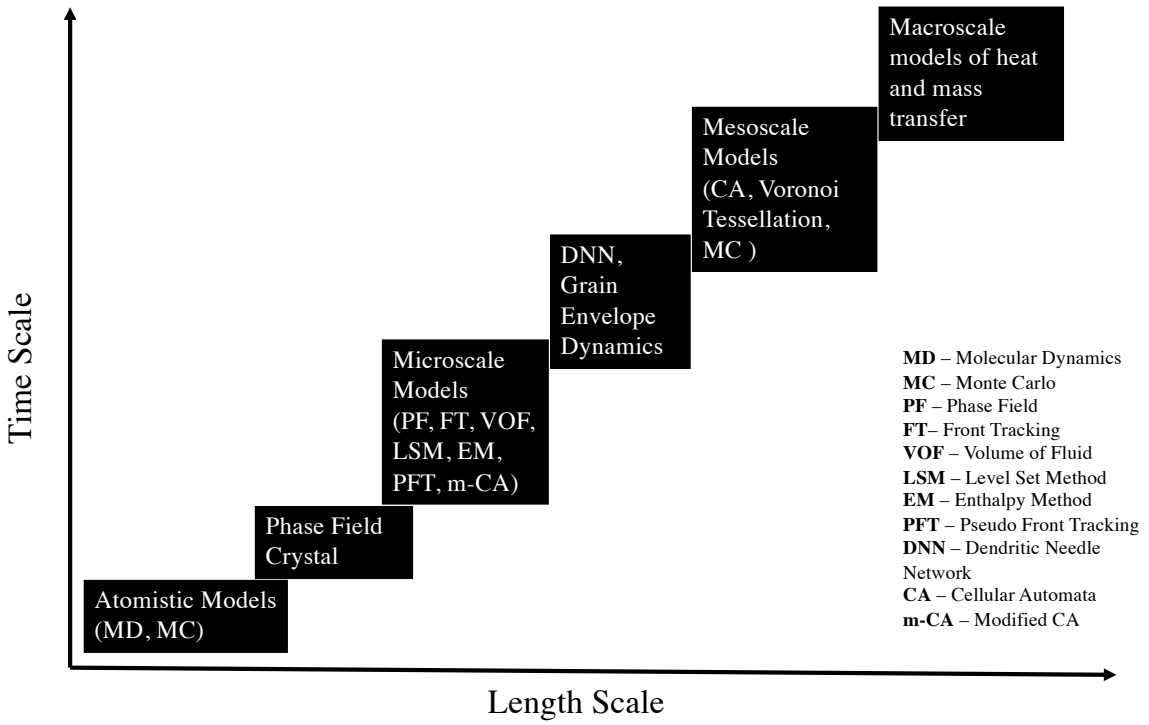

Figure 2.9: Different models used in the solidification study classified according to the domain of applicability.

are crucial in studying the microstructure formation over a wide range of processing conditions [72, 73, 74, 75, 76]. Atomistic models have also been used to quantitatively study the phenomenon of solute trapping during rapid solidification and interface coalescence during the late stage solidification [77, 78]. To bridge the gap between the atomistic and continuum scale the phase-field crystal (PFC) models were developed. PFC models describe the phenomenon at atomic length and diffusive time scale and have been used to study phenomena like an expansion on melting, solid-liquid bulk modulus, grain boundary energetics, reconstructive phase transitions and many more [79, 80, 81].

On a micro/mesoscale level, phase-field models have been extensively used to

study the evolution of solidification microstructure in a wide range of alloy systems. Interfacial free-energy anisotropy derived from atomistic models can be used as inputs in the phase-field models to predict the dendritic growth kinetics and orientation selection [82, 83]. In turn, the grain growth kinetics derived from the phase-field models can be used as inputs in the meso/micro-macro models of solidification such as Cellular Automata coupled with Finite Element (CAFE) and analytical models that make the connection between the microstructure and process scale [84]. In the subsections that follow, we will discuss the microstructure and grain-structure models in detail along with the Dendritic Needle Network (DNN) model which has been developed to bridge the gap between these two modelling approaches.

2.3.1 Microstructure Modelling

Over the last three decades, several numerical models have been developed to simulate the evolution of dendrites in pure metals and alloys under a wide variety of processing conditions. These numerical models can be generally classified into two different categories depending on how the moving solid-liquid interface is represented and tracked during the simulations: explicit and implicit interface tracking methods.

In explicit methods such as Front Tracking (FT) and Pseudo Front Tracking (PFT) methods, the interface is explicitly tracked by using the discretized form of the Stefan boundary condition. These methods usually rely on two different grids: a fixed Eulerian grid to solve the field equations and a lower order Lagrangian deforming grid that is used to keep track of the interface [85, 86]. The explicit interface tracking methods are computationally very expensive (equally or more expensive than phase field), the topological changes are not easy to handle and they are extremely difficult

to extend to 3D. To overcome these challenges implicit interface tracking methods were developed [87].

Implicit tracking methods such as Phase Field (PF), Volume of Fluid (VOF), Level Set Method (LSM) and Enthalpy Method(EM) use an auxiliary variable which is a function of space and time defined over the whole domain to describe whether a given location is solid or liquid [88, 89, 90, 91]. The auxiliary variable (order parameter) takes on a fixed but different value in the solid and the liquid domain, and a sharp and localized change in the order parameter is used to describe the solid-liquid interface. The approach avoids the complexity of applying the boundary condition at an unknown location which is part of the solution and topological changes are easier to handle. The main challenge in the implicit methods is to accurately relate the evolution of the order parameter with problem definition [82, 87]. Among all the methods used for microstructure evolution, the phase-field method has emerged as a top runner and is widely used to study the solidification phenomenon.

Phase Field Model

The phase-field (PF) model has its origins in the diffuse interface theory of van der Waals, Chan-Hilliard, and Ginzburg-Landau theories of phase transition [92, 93]. The PF model uses a non-conserved constant phase variable to describe the phase of the material and the solid-liquid interface is defined as a steep, but continuous transition of the phase-field variable [82]. The governing equations describing the evolution of the PF model ensures the minimization of the free energy of the system with time, moreover, they are coupled with the diffusion field near the interface [40].

PF models have been extensively used to study many different aspects of the

solidification and crystal growth phenomenon. Beginning with Kobayashi's works in 1987, there has been great interest in the PF method for simulating dendritic growth [40]. Following Kobayashi's work [94], the PF theory was soon extended to alloy systems and directional solidification [95, 96, 88, 97, 98, 99].

The PF methods were initially limited to high supersaturations, where the length of the diffusion boundary layer is small. The requirement that the width of the diffuse interface be the same as the physical interface posed a difficulty in making quantitative predictions with the PF method. With the development of asymptotic analysis of the phase-field variables known as the thin interface limit, it has become possible to perform quantitative predictions with the phase-field method. The thin interface limit allows one to use a much thicker interface than previously possible and helps in the elimination of the non-equilibrium effects at the interface [100, 101, 102]. The introduction of an anti-trapping current technique to avoid the problem of excessive solute trapping associated with a diffuse interface made it possible to make quantitative predictions for non-isothermal alloy solidification [100, 102]. Recently, progress has been made to develop quantitative PF models using the anti-trapping current technique that are valid for arbitrary phase diagrams and/or finite solute diffusivity in solid [70].

Karma and Rappel used PF models to test the microscopic solvability theory and have found good agreement at low anisotropies [40]. The PF model quantitatively agrees with directional solidification experiments [102] and provide an exact benchmark for analytical models of tip undercooling selection. The existence of stability gap in pattern selection at low interfacial anisotropies and origin of side-branching as noise amplification was also confirmed using the PF modelling [103, 104, 105]. The

approach has also been applied to multiphase problems and peritectic alloys [106, 107].

Recently, some researchers have applied PF modelling to predict the microstructure evolution during the PBF process. The thermal field and melt pool information were either calculated using macroscopic models of heat and fluid flow (Finite Element, Lattice Boltzmann, Volume of Fluid) or through the analytical models and were used as input to the PF method to predict the effect of processing parameters on the microstructure, growth morphology and microsegregation patterns during the PBF process. The phase-field models were validated by comparing the grain structure and dendritic spacing with the experimental micrographs [108, 109, 110, 111, 112, 113, 114, 115, 116]. However, the PF method has certain limitations. It is computationally very expensive and additional techniques such as asymptotic analysis and anti-trapping current are required to make quantitative predictions.

2.3.2 Grain Structure Modelling

Stochastic models based on Cellular Automata (CA) and Monte Carlo (MC) methods can be used to predict the grain structure and texture during the solidification process. Compared to the models discussed in the previous section, these models do not resolve the individual dendritic crystals but rather simulate the growth of the dendritic envelope using simple rules and growth kinetics derived from analytical models (not in the case of MC). With the improvements in the computational implementation, CA models can simulate grain structure in large castings within reasonable computational times. In what follows we will discuss the CA model in detail [117, 118, 119, 120].

Cellular Automata

In CA, the discrete computational domain is represented by a grid of cells having defined states and the evolution of the system is governed by state transition rules that depend on the cell neighbours. Complex behaviours and patterns can be simulated by repeatedly applying the transformation rules [121].

CAFE model was developed by Rappaz and Gandin in the 1990s to simulate the dendritic grain formation during solidification [117, 118]. CAFE models have been successfully applied to study casting, directional solidification, grain structure formation, columnar to equiaxed transition (CET), grain impingement and defect formation in different alloy systems [117, 118, 122, 123]. CAFE models have also been used to study the grain structure and texture formation during MAM process [124, 125, 126, 127, 128].

Although the CAFE model has been successfully applied to study numerous phenomena associated with solidification with great success. However, its application is limited by certain assumptions made during the modelling process. The grain growth kinetics is taken from the analytical model and therefore it is restricted only to cases for which analytical growth theory exist. In the CAFE model, the dendrites are restricted to grow along the $\langle 100 \rangle$ directions and as such it does not apply to hexagonal systems. Moreover, the grains in the CAFE model interact through hard-impingement and the grains do not slow down when their solute fields overlap [84].

To overcome some of the restrictions of the CAFE model, the modified-Cellular Automata (m-CA) model was developed. These m-CA model solves for the solute field and thus can handle soft impingement. This model can also elucidate the underlying dendritic structure inside the grain envelope. The m-CA model has been

successfully used to predict the primary and secondary dendritic arm spacing, CET, growth competition among dendritic trunks and MAM process [129, 130, 131]. Although m-CA overcomes some of the limitations of the CAFE model and produces dendritic structures like PF, however, the growth algorithm cannot predict the actual kinetics of the dendrite tips and has never been validated against analytical solutions or phase field computations. To get to PF accuracy, the m-CA model needs a finer grid and refined algorithm for calculating the interfacial curvature [84].

2.3.3 Dendritic Needle Network

Dendritic Needle Network (DNN), which represents the hierarchal dendritic structures as thin needles that interact through long-range diffusion field has been developed to bridge the gap between micro-scale models such as PF and mesoscale models such as CAFE. In the DNN model, the solid-liquid interface is assumed to be in local equilibrium. The growth dynamics of the individual needle is uniquely defined by combining the solute balance near the tip region and the standard microscopic solvability condition. However, in its current form DNN model is restricted to only simulating grain growth in low Péclet number regime [132, 133].

2.3.4 Cellar Array Growth Model

An alternative approach to study interfacial characteristics during directional solidification is through the use of the cellular array growth model developed by Hunt et al. [134, 135, 1, 136, 2, 3]. The numerical model uses a hexagonal grid to represent an array of directionally grown cells and dendrites and can be used to study the effect

of the input parameters such as applied thermal gradient and steady-state interfacial velocity and material properties on the existence of the cellular and dendritic structures during directional solidification of binary alloys. The model has been used by the Hunt et al. to study the growth morphology, stable spacing range, interfacial conditions and microsegregation profile for a range of solidification velocities going from normal solidification to rapid solidification conditions.

In comparison to the phase-field model which is very computationally expensive and requires additional techniques such as anti-trapping current and asymptotic analysis to make quantitative predictions and the DNN model which is only restricted to solidification done at low velocities, the cellular array growth model can be used to study interfacial characteristic from the onset of constitutional undercooling to absolute stability limit. In this thesis, a model based on the work of Hunt et al. has been used to study relationship between the MAM processing conditions and the interfacial conditions at the solid-liquid interface to establish if the MAM process exhibit a rapid solidification route.

In the chapters that follow, the scope and objectives of this thesis are discussed. This is followed by a detailed description of the developed model and its application to the binary Al-Cu alloy system to study the interfacial characteristics over a range of growth velocities.

Chapter 3

Scope and Objective

There has been an increase in the use of the MAM especially PBF-L and PBF-EB processes in the aerospace and the medical industry. However, the parts made by MAM have large structure and property variations which makes their widespread adoption difficult. Moreover, it is generally assumed in the literature that the solidification during MAM follows the rapid solidification processing route, however, there are not many studies where the interfacial conditions during the PBF process have been systematically studied.

To address these issues and to quantify the interfacial conditions during the PBF process, in this master's project it is proposed to develop a computationally efficient model to simulate the growth of the cellular and dendritic array during the PBF process.

The newly developed model is based on the work of Hunt et al. [134, 135, 1, 136, 2, 137, 3]. The model accounts for the changes in the phase diagram and other non-equilibrium phenomena that occur at high interfacial velocities and is capable of simulating an array of directionally grown dendrites or cells at both low and high

Péclet numbers.

The objectives of this study are as follows:

1. To develop a computationally efficient model of direction solidification that is valid at both low and high Péclet numbers.

2. To quantify the interfacial conditions such as undercooling values, tip concentration and tip radius during the PBF-L process.

3. To identify the range of possible primary spacing during the PBF-L process.

4. To identify the RS processing zone based on the tip/spacing Péclet number during the PBF-L process.

Chapter 4

Numerical Method

In this chapter, the numerical method that has been developed to study the interfacial behaviour during the PBF-L process is described in detail. The model can simulate an array of directionally grown cells or dendrites under steady-state growth conditions. In the model, a directionally grown array of cells or dendrites are approximated using a grid of hexagonal cells and henceforth referred to as the cell model.

The cell model solves the solute conservation equation in an externally applied linearly moving temperature field. In the cell model, the shape of the solid-liquid interface is not known a priori and needs to be identified as part of the solution. The developed model accounts for the constitutional and curvature undercooling, along with the variation of partition coefficient and diffusion coefficient with temperature. At high growth velocities, the non-equilibrium effects such as the variation of the partition coefficient and liquidus slope with velocity and interface attachment kinetics are also considered in the present model. The model is used to estimate the range of primary spacing, the extent of different undercooling values, and the tip and spacing Péclet number for a range of growth velocities during the PBF-L process. In what

follows the cell model is described in detail.

4.1 Model Description

In the cell model, an axisymmetric hexagonal grid is used for representing an array of directionally grown cells or dendrites. As shown in Figure 4.1a, the hexagonal grid consists of a representative repeat unit, where each cell of radius/width W is surrounded by six other cells and so on. The distance between centres of any two adjacent cells is $2W$ and is equal to the primary spacing λ_1. Each cell in the array consists of a steadily growing cell or dendrite with a constant tip velocity V into a liquid of bulk composition C_0 as shown in Figure 4.1b [134, 135]. Due to symmetry, only a single half-cell from the array is modelled and its interaction with the neighbouring cells is accounted via appropriate boundary conditions. The single half-cell used in the simulations is shown in Figure 4.2. In the Figure 4.2, the surface Γ_4 is the solid-liquid interface which is a free-boundary of the domain and its shape needs to be identified as part of the solution. However, to simplify the free-boundary problem, it is assumed that the solid-liquid interface can be represented as a paraboloid i.e., a surface of revolution. The coupling between the shape of the solid-liquid interface and the governing partial differential equation for the steady solidification problem results in a set of nonlinear equations. To keep the nonlinear problem tractable, further simplifying assumptions are made such that no diffusion is considered in the solid phase and the temperature field is externally applied which has an imposed translation in the z-direction. Under these assumptions, the problem reduces to identifying the shape of the interface and position of the tip in an external temperature field such that the conservation equation (Eq. 4.3.1 and Eq. 4.3.3) is satisfied everywhere

in the domain and the undercooling condition (Eq. 4.6.3) is satisfied everywhere at the solid-liquid interface.

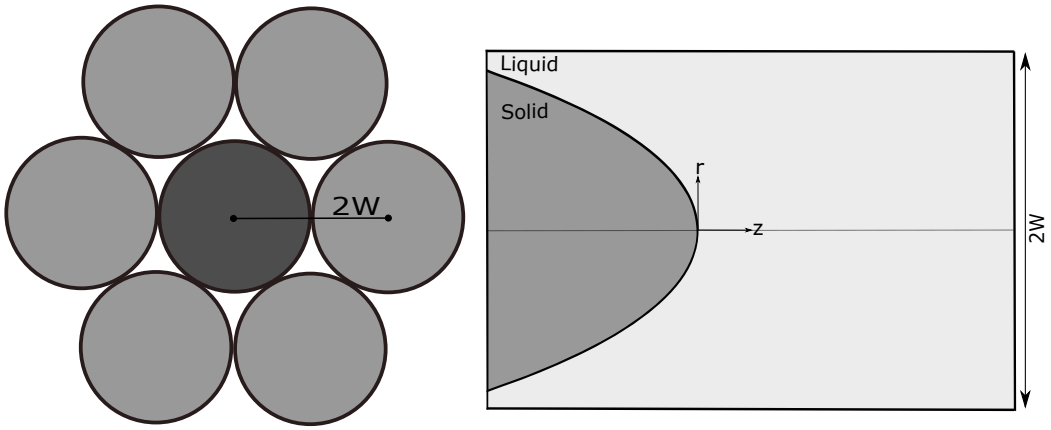

(a) (b)

Figure 4.1: a) Schematic representation of the cellular/dendritic array when viewed from the growth direction. In the simulations, only the middle dark grey cell is modelled. The distance between the centres of any two adjacent cells is $2W$ and is equal to the primary spacing λ_1. b) A single cell from the grid with the growing solid inside.

4.2 Governing Equations and Boundary Conditions

The governing equation for the cell model consists of the solute conservation equation in the liquid domain, which is solved with appropriately defined boundary conditions at the fixed and free domain boundaries. As mentioned previously, the coupling between the shape of the interface and the field variable, along with the boundary conditions results in a system of nonlinear equations. In the present work, the resulting system of nonlinear equations is simultaneously solved for the interface shape and the concentration profile using the Newton-Raphson method.

Given the axisymmetric nature of the problem, it is easier to work in a cylindrical

coordinate system and the solute conservation equation in the liquid domain in a cylindrical coordinate system can be expressed as

$$\frac{\partial C_l}{\partial t} = D_l \nabla^2 C_l, \tag{4.2.1}$$

Since steady-state solutions are of interest in the present work, it is better suited to work in a unidirectional moving frame of reference which is moving with velocity V in the axial direction. Under steady-state conditions and in a moving frame of reference the Eq. 4.2.1 can be rewritten as

$$D_l \nabla^2 C_l + V \frac{\partial C_l}{\partial z} = 0, \tag{4.2.2}$$

where C_l is the composition in the liquid phase, D_l is the solute diffusivity in the liquid phase, and V is the steady-state tip velocity.

Two distinct boundary conditions are required at the free-boundary of the domain. One of the conditions is required to satisfy the solute conservation equation whereas the other condition is required to identify the shape of the free boundary. Interface being the free-boundary, one of the conditions is given the Stefan condition. In the absence of diffusion in the solid phase, the solute flux at the solid-liquid interface is given by one-sided Stefan condition as

$$V_n(1-k)C_l^* = -D_l \frac{\partial C_l}{\partial n}, \tag{4.2.3}$$

where V_n is the normal interfacial velocity, k is the partition coefficient, C_l^* is the interfacial composition on the liquid side and $\frac{\partial C_l}{\partial n}$ is the normal solute flux at the interface. The above equation was used to satisfy the solute conservation equation in

the present model.

The other condition at the solid-liquid interface, which was used to identify the self-consistent shape, is given by an equation that relates the interfacial temperature with the interfacial composition and curvature and can be expressed as

$$T^* = T_L + m(C_l^* - C_0) - \Gamma(\zeta K_1 + K_2), \tag{4.2.4}$$

where T^* is the interfacial temperature, T_L is liquidus temperature, m is liquidus slope, C_0 is initial composition, Γ is Gibbs-Thomson coefficient. K_1 and K_2 are the two principal curvatures of the surface of revolution and ζ is a parameter that accounts for the anisotropic interfacial energy. ζ is given as

$$\zeta = 1 - 15\epsilon\cos(4\theta),$$

where ϵ is the anisotropy parameter which is a measure of the strength of the anisotropy. The surface energy is assumed to have four-fold symmetry and θ is the angle between the surface normal and the crystal axis.

In addition to this, the governing equation also needs to satisfy the conditions at the domain boundaries. At the north wall of the domain (Γ_1) and the axis of symmetry (Γ_3), a no flux condition was specified i.e.,

$$\frac{\partial C_l}{\partial r} = 0. \tag{4.2.5}$$

At the far end of the domain i.e., $z \to \infty$, the concentration will be equal to the bulk concentration C_0 . However, for this condition to be applicable in the simulation, the east wall (Γ_2) needs to be very far away from the tip. Alternatively, at a far enough

distance from the tip, there will be no compositional variation in the r-direction and under such assumption, the Eq. 4.2.2 can be integrated to give the concentration gradient at the east wall (Γ_2)

$$\frac{dC_l}{dz} = -\frac{V}{D_l}\big(C_l(z) - C_0\big), \tag{4.2.6}$$

where $C_l(z)$ is the liquid composition at a distance z ahead of the tip. Please note that the above equation is valid if the distance $L_2 > D_l/V + W$ [134].

Finally, the boundary condition at the west wall (Γ_5) is obtained by assuming the complete mixing at the base of the interdendritic region. This condition is given as

$$\frac{dC_l}{dz} = \frac{G}{m}. \tag{4.2.7}$$

The above equation is necessary to satisfy the Eq. 4.2.4 at the base of the cell/dendrite. This assumption is valid if $L_1 >> (VW^2)/D_l$ [134].

As mentioned previously, no heat flow is considered in the present model and a linearly moving temperature field is externally imposed in the simulations. The temperature field moving with velocity V in the z-direction is expressed as

$$T = G(z - Vt), \tag{4.2.8}$$

where G is the thermal gradient and t is time. The temperature field is imposed in the simulations by translating to a moving frame of reference by arbitrary fixing the liquidus isotherm at the origin i.e.,

$$T = Gz + T_L.$$

Under these conditions, the problem reduces to identify the shape of the interface and the position of the tip with respect to the liquidus isotherm such that the solute conservation equation is satisfied everywhere in the domain and the undercooling equation is satisfied everywhere at the interface.

4.3 Discretization

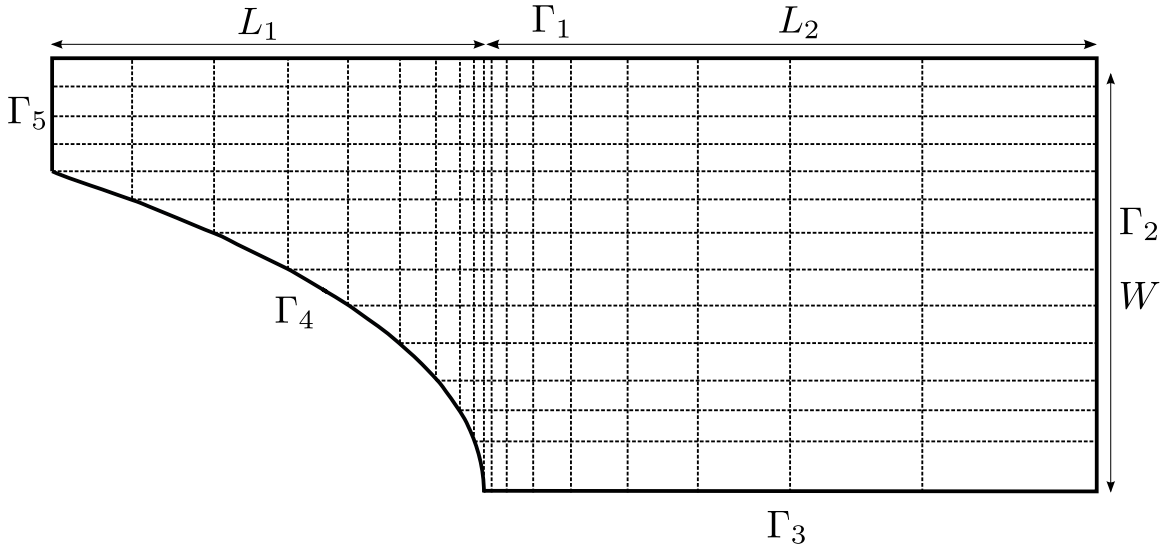

Figure 4.2: An illustration of the computational domain and the grid used in the simulations. The growth direction is horizontal and towards the right; the length of the cell behind the tip is L_1 while L_2 is the length ahead of the tip. Finally, the domain boundaries are denoted by Γ_i where Γ_4 is the free boundary of the domain and the rest are the fixed boundaries.

The numerical model is developed in the cylindrical coordinate system following the finite volume approach. For this purpose, the complete computational domain is divided into several small control volumes (CVs) as shown in Figure 4.2. The procedure for generating the grid will be outlined in the section 4.4. The governing equation is discretized by considering the accumulation of the solute in a given control

volume. Under steady-state conditions, the influx will be equal to the outflux and no accumulation will take place in a control volume. Using the divergence theorem, the discretized equation for the internal control volume can be written as

$$A_e\left(D_l\frac{\partial C_l}{\partial z}+VC_l\right)_e - A_w\left(D_l\frac{\partial C_l}{\partial z}+VC_l\right)_w + A_n\left(D_l\frac{\partial C_l}{\partial r}\right)_n - A_s\left(D_l\frac{\partial C_l}{\partial r}\right)_s = 0, \tag{4.3.1}$$

where the subscripts e, w, n, s represents the east, west, north and south wall of a CV respectively. A_k, where $k = \{e, w, n, s\}$ represents the area of the corresponding CV wall. The concentration gradient and its value at the north and south wall are calculated using the central differencing, whereas, exponential interpolation is used for the east and west wall due to the presence of convective fluxes in the z direction [138, 139]. The form of the exponential interpolation is given as [135]

$$C = A + B\exp\left(\frac{-Vz}{D_l}\right) \tag{4.3.2}$$

The constants A and B are calculated using the values of the adjacent control volume.

Similarly, the discretized equation for the interfacial CV is expressed as

$$A_e\left(D_l\frac{\partial C_l}{\partial z}+VC_l\right)_e + A_n\left(D_l\frac{\partial C_l}{\partial r}\right)_n - A_i\left(D_l\frac{\partial C_l}{\partial n}+V_nC_l\right)_i = 0, \tag{4.3.3}$$

where A_i is the area of the interfacial surface and $\frac{\partial C_l}{\partial n}$ is the normal solute flux at the interface, which is estimated using the Stefan condition.

4.4 Interface Representation and Grid Generation

Before a grid can be generated, a method is required to discretely represent the shape and location of the unknown solid-liquid interface. Various approaches such as height function, line segment and marker particles exist to represent an unknown boundary in a free-boundary problem. Each method has its advantages and disadvantages, and in the present work, the height function method is used to represent the unknown solid-liquid interface [140]. In the height function approach, the unknown boundary is represented using a discrete set of points $(z, r(z))$, where $r(z)$ is the height of the interface at a distance z behind the tip.

The height function approach is extremely efficient and easy to implement in a numerical model. However, the height function method requires the boundary slope to be less than the mesh cell aspect ratio to work well. Furthermore, it cannot be used for multiple-valued surfaces i.e., modelling secondary and tertiary arms. [140].

The solution to the above solidification problem necessitates the use of very small control volumes to accurately resolve the area near the tip region. Whereas, larger control volumes can be used further away from the tip. Therefore, to achieve higher computational efficiency a nonuniform structured grid is used in the cell model as shown in Figure 4.2.

For the easy treatment of the interfacial control volume cells for discretization and the application of boundary conditions, the grid is generated in such a way that the interfacial control volume corners lie on the interface. To calculate the interfacial area, if the interface CVs are small or if the interface curvature is less, the interface passing through the control volume corners can be approximated using the CV diagonals.

In Hunt et al.'s model, a geometric progression was used to distribute the grid

points in the axial direction [1]. However, as the number of grid points $\rightarrow \infty$ the grid size does not go to zero for a grid generated using a geometric progression [141]. To overcome this issue, an interpolating scheme is used in the present work to distribute the grid points in the axial direction (along z). The axial coordinates of the grid points are generated in two steps. In the first step, the length behind the tip L_1 is divided into m points by using a mapping between a uniform computational domain going from $[0, 1]$ and the physical domain going from $[0, L_1]$. This mapping is expressed as

$$z = L_1 \left(\frac{(\beta + 1) + (1 - \beta) X^{1-x^c}}{X^{1-x^c} + 1} \right) \tag{4.4.1}$$

and

$$X = \frac{\beta + 1}{\beta - 1},$$

where $x^c \in [0, 1]$ is the distance in the computational domain and β is a factor that controls the distribution of points along the axis. If $\beta \rightarrow 1$, the points are clustered near the origin [139]. In the second step, the distance in front of the tip L_2 is divided into n points using the same methodology on the physical domain going from $[0, L_2]$. At this point, the complete domain is divided using vertical lines.

Now, the radial coordinates of the intersection of grid lines are determined. Along the solid-liquid interface Γ_4 the coordinates are given by the intersection of the vertical lines with the interface. Finally, the remaining area above the interface Γ_5 is divided into k equal points. For most of the simulations, $m = 20$, $n = 40$, $k = 10$ points were used to generate the grid with $\beta = 1.0005$. The axial coordinates of the grid points are kept fixed throughout the simulation. However, as the interface changes during

the process of reaching a convergent solution, the values of $r(z)$ change, and thus the vertical coordinates are updated each iteration. This ensures that the interface always passes through the control volume corner and no explicit redistribution of grid points is required after each iteration.

4.5 Interface Reconstruction

To apply the boundary conditions at the interface, the interface normal vector is required for the Stefan condition Eq. 4.2.3, and the principal curvatures are required for the application of the undercooling Eq. 4.2.4. The Stefan condition is applied at the centroid of each interface control volume. Whereas, the undercooling equation is applied at each interface control volume corner (interface grid points) by linearly interpolating/extrapolating the compositional values from the adjacent interfacial control volume cells.

The normal vector is calculated using the formula

$$\hat{n} = \frac{1}{\sqrt{r'^2 + 1}} \begin{bmatrix} -r' \\ 1 \end{bmatrix}, \tag{4.5.1}$$

and the principal curvatures for a surface of revolution given by the generating curve $r = r(z)$, where z is the distance along the axis of revolution can be expressed as

$$K_1 = \frac{r''}{(1 + r'^2)^{\frac{3}{2}}} \tag{4.5.2a}$$

$$K_2 = \frac{-1}{r\sqrt{1 + r'^2}} \tag{4.5.2b}$$

where r' and r'' represents the first and second derivative respectively.

To calculate the first and second derivatives at any interface grid point, different approaches such as finite differencing and cubic spline interpolation were tried in this study. The above two methods were used to calculate the derivatives of a surface of revolution given by $r = \sqrt{-z}$, where $z < 0$ and the resulting values were compared against the analytically obtained values. As shown in Figure 4.3, finite differencing approximation and the cubic spline interpolation suffer from instabilities in the region of high gradients i.e., near the tip and resulting values have a large error in them.

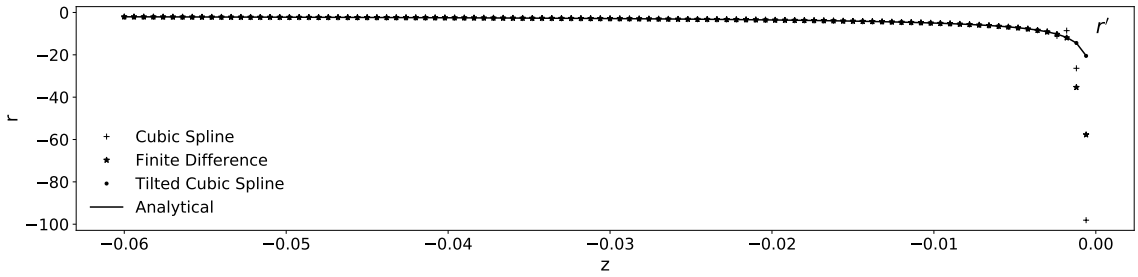

(a)

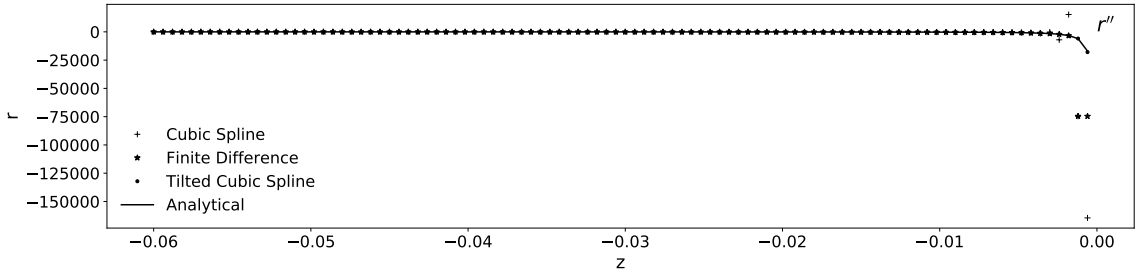

(b)

Figure 4.3: Comparison of a) first and b) second derivatives calculated using the finite differencing approximation, cubic spline interpolation and tilted cubic spline interpolation (the cubic spline was fitted in a co-ordinate frame which was rotated at an angle of 45^o w.r.t to the original coordinate frame) with the analytically obtained values for a surface of revolution given by $r = \sqrt{-z}$ where $z < 0$.

To avoid instabilities in the cubic spline interpolation near the tip region, the cubic spline is fitted in a co-ordinate system which is rotated at 45^o with respect to the original frame of reference. The interface grid point coordinates from the original coordinate system can be mapped to the rotated coordinate system via 2×2 rotation matrix. The rotation matrix can be expressed as

$$\begin{bmatrix} \tilde{z} \\ \tilde{r} \end{bmatrix} = \begin{bmatrix} \cos(\theta) & -\sin(\theta) \\ \sin(\theta) & \cos(\theta) \end{bmatrix} \begin{bmatrix} z \\ r \end{bmatrix}, \tag{4.5.3}$$

where $(z,\ r)$ is a coordinate of a point in the original coordinate system whereas $(\tilde{z},\ \tilde{r})$ is the corresponding coordinate in a new coordinate system which is rotated at an angle θ with respect to the original one. Now, the derivatives in the original coordinate system can be related to the derivatives in the rotated coordinate system using the above rotation matrix. The relationship between the first derivatives is given as

$$r' = \frac{\tilde{r}' - 1}{\tilde{r}' + 1}, \tag{4.5.4}$$

and the relationship between the second derivatives is expressed as

$$r'' = \frac{\tilde{r}''(1 + r'^2 - 2r')}{\sqrt{2}(1 + \tilde{r}')}, \tag{4.5.5}$$

where $\tilde{r}'$ and $\tilde{r}''$ are the first and second derivatives in the new coordinate system. Although the principal curvatures of a surface remain invariant under rotation, Eq. 4.5.2b is only valid when the surface of revolution is represented by a generating

curve $r = r(z)$ where the z direction coincides with the axis of the revolution. Therefore, the derivatives from the rotated coordinate system are transformed back to the original coordinate system in order to calculate K_2 using Eq. 4.5.2b.

Please note that special treatment is required to calculate the principal curvatures at the tip since Eq. 4.5.2b is undefined because $r = 0$ at the tip, and also to avoid any error in the derivatives due to cubic spline boundary condition. The first issue is resolved by taking note of the fact that the two principal curvatures at the tip of a regular surface of revolution are the same and equal. Now to resolve the second issue, since it is not required to calculate K_2, one can take advantage of the fact that the principal curvatures of a surface remain invariant under rotation, and also the Eq. 4.5.2a for calculating K_1 remains valid under rotation. Following this, a small region near the tip is mirrored and a cubic spline is fitted to the mirrored region by changing the independent and dependent variables. This enables the direct calculation of K_1 from the mirrored and rotated cubic spline interpolation and thereby avoiding any errors due to cubic spline boundary conditions.

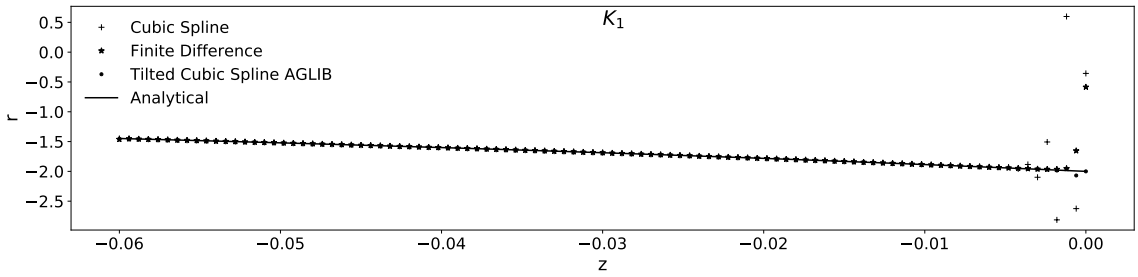

(a)

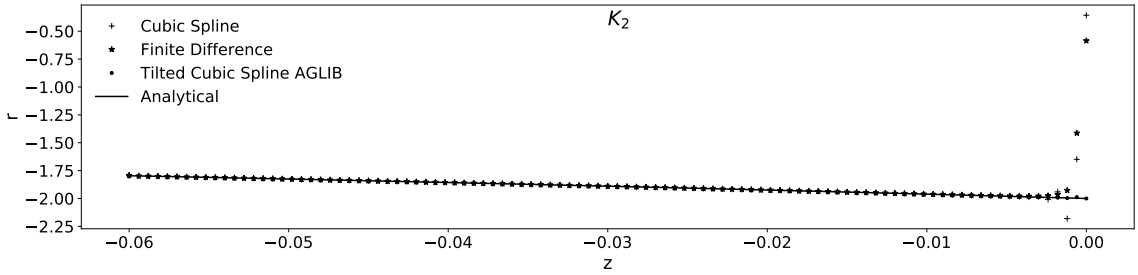

(b)

Figure 4.4: Comparison of a) first principal and b) second principle curvatures calculated using the finite differencing approximation, cubic spline interpolation and tilted cubic spline interpolation with the analytically obtained values for a surface of revolution given by $r = \sqrt{-z}$ where $z < 0$. Please note that in the case of tilted cubic spline, the curvature at the tip was calculated by fitting a separate cubic spline in the tip region as described in the text.

The interface normal and curvature values obtained using the three approaches i.e., finite differencing, cubic spline interpolation and tilted cubic spline interpolation are shown in the Figure 4.3 and Figure 4.4 respectively. The results from the three methods are compared with the values obtained analytically for a surface of revolution given by $r = \sqrt{-z}$, where $z < 0$. As evident from the figure, the tilted cubic spline interpolation along with the special treatment of the tip results in a very good estimation of the interface normal and curvature values even in the region of high gradients. Please note that the result of the cubic spline interpolation is sensitive to the boundary condition used. In the model, the cubic spline is fitted using the

AGLIB library with the default boundary condition [142].

4.6 Model Application to Rapid Solidification

The model described so far does not account for any non-equilibrium phenomenon that takes place at high growth velocities, therefore, the model is only applicable to low Péclet number regime i.e., solidification done at normal growth velocities. At high growth velocities, the above model needs to be modified to account for the variation of the partition coefficient and the liquidus slope with the growth velocity. In addition to this, at high growth velocities the kinetic undercooling can be significant and therefore the interfacial attachment kinetics also need to be incorporated in the model [26, 3, 9].

In addition to this, the numerical model was also modified to have a more realistic representation of the phase diagram instead of the linear approximation. This was done by parametrizing the liquidus and solidus line via polynomial equation giving $T_l(C)$ and $T_s(C)$. Thus, the partition coefficient also varies with temperature i.e., $k_e = k_e(T)$.

The variation of the partition coefficient with growth velocity is expressed as [26]

$$k_v = \frac{k_e(T) + (\delta_i V/D_i)}{1 + (\delta_i V/D_i)}, \tag{4.6.1}$$

where k_v is the velocity-dependent partition coefficient, k_e is the equilibrium partition coefficient, δ_i is the inter-atomic width which is of the order of the thickness of the interface and D_i is the interface diffusivity coefficient. The variation of the partition coefficient at the solid-liquid interface was considered by taking into account the temperature and normal velocity at the interfacial location.

At high growth velocities, the equilibrium phase diagrams are not applicable and the relationship between the kinetic liquidus composition C_l^i and the equilibrium liquidus composition C_l^e is expressed as [9, 3]

$$C_l^e = C_l^i\left(1 + \frac{k_e - k_v(1 - \ln(k_v/k_e))}{1 - k_e}\right) + \frac{V}{V_0(1 - k_e)}, \tag{4.6.2}$$

where V_0 is a parameter which is of the order of the velocity of sound. The first term in the above equation takes into consideration the variation of the equilibrium liquidus slope with the interface velocity and the second term accounts for the linear attachment kinetics. C_l^i is calculated at the interface grid points by interpolating/extrapolating the compositional values from the adjacent interfacial control volumes. Using C_l^e, the interfacial temperature can then be determined as

$$T^* = T_l(C_l^e) - \Gamma\big(\zeta K_1 + K_2\big) \tag{4.6.3}$$

In the rapid solidification model, the diffusion coefficient was assumed to vary with the temperature as

$$D_l = D_0 \exp(-Q/R_g T), \tag{4.6.4}$$

where D_0 is the diffusivity constant, Q the activation energy and R_g the gas constant. Please note that in the model, $D_i = D_l(T_L)$, since interface diffusivity coefficient is unknown. At any step of the simulation, the temperature-dependent diffusivity i.e., $D_l(T)$ was assumed to be equal in every CV and calculated based on the tip temperature.

4.7 Solution Methodology

The above problem was formulated as a system of nonlinear equations and simultaneously solved for the interface shape and the composition profile using the PETSc's line search variant of Newton's method [143, 144, 145]. Newton's method is a powerful technique for solving a system of nonlinear equations and has q-quadratic convergence if the initial guess is close to the solution and the Jacobian is non-singular. However, if the starting guess is not close to the solution, Newton's method may or may not converge to a solution. Globally convergent variants of Newton's method such as line search and model-trust region approaches were introduced to overcome the issue of local convergence. These methods use specific criteria to decide the step direction and length to compute the next successive step when the Newton step is not acceptable [146, 147].

In addition to the good initial guess, Newton's method also requires an accurate estimation of the Jacobian matrix for quadratic convergence. The Jacobian matrix can be either computed analytically or estimated using numerical approximations [146]. Analytical calculation of the Jacobian matrix of a free-boundary problem can be very tedious and error-prone. Even a small error in the Jacobian matrix can deteriorate the performance of Newton's method or may even cause it to diverge. In contrast, numerical estimation of the Jacobian matrix is computationally expensive and since the grid is tightly coupled with the problem, as the interface evolves the Jacobian needs to be recomputed at every iteration.

Initially, an analytically calculated Jacobian matrix was used in the present work. The analytical estimation of the Jacobian matrix posed a challenge since the interface normals and curvatures were calculated using the cubic spline interpolation during

the function evaluation. Since the coefficients of the cubic spline interpolation were unknown, the function could not be analytically differentiated to calculate the Jacobian matrix. To overcome this issue, finite difference approximations for the interface normal and curvature calculation were used during the analytical Jacobian estimation. The correctness of the analytically calculated Jacobian matrix was tested by calculating the direction derivatives using the analytical Jacobian matrix and comparing it with the values obtained from the fundamental theorem of calculus. This test can be written as

$$J(\mathbf{x}).\mathbf{p} = \lim_{\delta \to 0} \left[\frac{F(\mathbf{x} + \delta\mathbf{p}) - F(\mathbf{x})}{\delta} \right] \tag{4.7.1}$$

where $F(\mathbf{x})$ is some vector valued function, $J(\mathbf{x})$ is its Jacobian matrix, $\mathbf{p}$ is the direction vector and $\delta > 0$ is as scalar. If the Jacobian matrix is correctly estimated then $E(\delta) = ||J(\mathbf{x}).\mathbf{p} - \delta^{-1}(F(\mathbf{x} + \delta\mathbf{p}) - F(\mathbf{x}))||_2$ will tend to zero.

Figure 4.5 shows the result of the above directional derivative test applied to the analytical Jacobian. For this test, two different approaches were used to estimate the interface normal and curvatures in the function evaluation, and their derivatives in the Jacobian matrix. In the case of Figure 4.5a, cubic spline interpolation was used in the function evaluation to calculate the interface normal and curvatures, whereas, their derivatives in the Jacobian matrix were calculated using the finite difference approximation. Whereas in the case of Figure 4.5b, finite differencing was used in both the function evaluation and the Jacobian estimation to calculate the interface normal and curvatures, and their derivatives. For this test, $\epsilon = 0$ i.e., no anisotropy in the surface energy was considered. In the case of Figure 4.5a, the error did not go down as the $\delta \to 0$, therefore, finite difference approximation

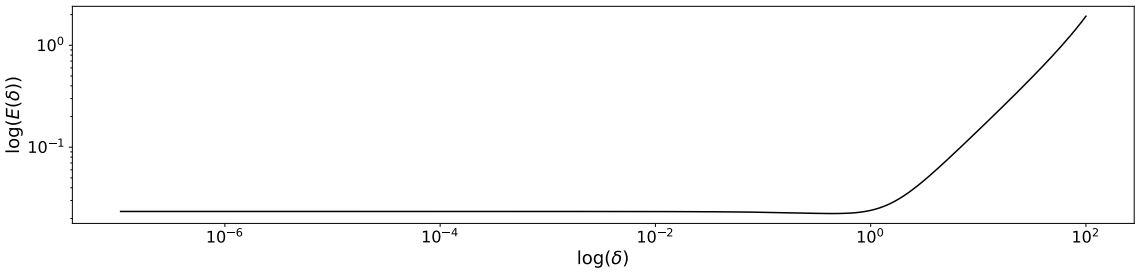

(a)

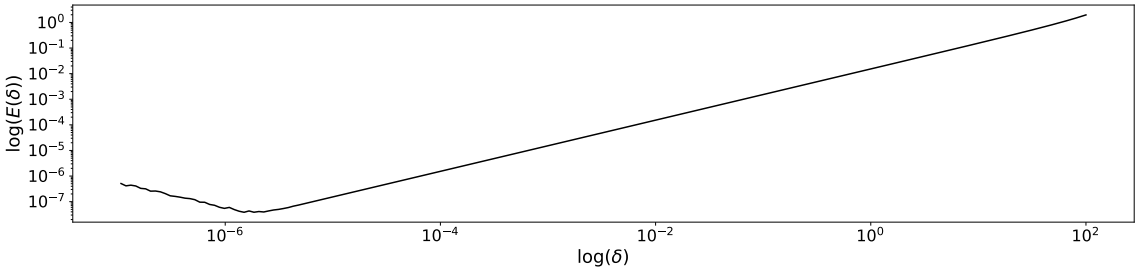

(b)

Figure 4.5: Result of the directional derivative test used to test the correctness of the analytical Jacobian matrix. In figure (a) cubic spline interpolation was used whereas in figure (b) finite difference approximation was used to calculate the interface normal and curvatures in the function evaluation. The interface normal and curvature derivatives in the Jacobian matrix were based on the finite difference approximation irrespective of the strategy used to construct the interface in the function evaluation.

cannot be used in the Jacobian estimation when cubic-spline is used to reconstruct the interface during function evaluation. To further confirm this, another directional derivative test was performed where finite differencing was used to reconstruct the interface in both the function evaluation and Jacobian estimation. The result of this test is shown in Figure 4.5b. Please note that the numerical instabilities due to floating-point operation causes the error to go up after a certain value of δ in the Figure 4.5b. Following this, no more attempts were made to analytically calculate the Jacobian matrix and the Jacobian was numerically estimated using the built-in

finite differencing approximation in the PETSc.

The guess solution for Newton's method is estimated using a two-step approach. In the first step, the initial shape of the interface is estimated using the equation proposed by McCartney and Hunt [134]. The equation is expressed as

$$g_l^{k_e-1} = \frac{(C_t + Gz/m)(1-k_e) + D_l G/mV}{C_t(1-k_e) + D_l G/mV}, \tag{4.7.2}$$

where C_t represents the tip composition and g_l is the liquid fraction at a distance z behind the tip. The tip composition can be calculated as

$$C_t = (C_0 - D_l G/mV) \tag{4.7.3}$$

and

$$g_l = 1 - \left(\frac{r}{W}\right)^2 \tag{4.7.4}$$

In the second step, with the initial estimate of the interface shape, the interface shape is fixed and a linear solve is done to estimate the initial composition profile. After this, the combined initial interface shape and solutal field are used as the starting guess for Newton's method. The solutions are iterated until the error in the composition values obtained from the conservation equation (Eq. 4.3.1 and Eq. 4.3.3) and the temperature values obtained from the undercooling Eq. 4.6.3 were less than 10^{-7} everywhere in the domain and along the solid/liquid interface respectively. Note that to prevent the line search method from stepping towards invalid interface shapes, i.e., when the interface height does not monotonically increase with the distance from the tip, an artificial cost is added in the functional evaluation. In addition to this for

certain cases, slowly turning on the anisotropy parameter in the undercooling equation from a very small value to the desired value can help in getting the convergence.

4.8 Material Parameters

In the next chapter, the cell model is applied to a binary Al-Cu alloy to identify the range of cell spacing W for which self-consistent interface exists for a given range of input parameters. The material properties of the Al-Cu system are listed in the Table 4.1 [3, 9].

Table 4.1: Physical constants for the Al-Cu system and other input parameters used for the simulations [3, 9].

D_0 (m^2/s)	1.10×10^{-7}
Q (J/mol)	23800
Γ (Km)	1×10^{-7}
δ_i (m)	0.9×10^{-9}
V_0 (m/s)	1000
E_4	0.005
C_0 (at%)	12.80
G (K/m)	5×10^6
$T_l(C) = 933.6 - 5.37 \times C - 0.34369 \times C^2 + 0.04315 \times C^3 - 2.2054 \times 10^{-3} \times C^4 + 3.7162 \times 10^{-5} \times C^5$	
$k(T) = 1.1317138 \times 10^4 - 66.910962 \times T + 0.15815355 \times T^2 - 1.8679168 \times 10^{-4} \times T^3 + 1.1023244 \times 10^{-7} \times T^{-7} - 2.6001967 \times 10^{-11} \times T^5$	

The liquidus slope can be calculated by taking the derivative of the $T_l(C_l)$ with respect to C_l.

Chapter 5

Results and Discussion

In this chapter, the numerical method developed in this thesis is applied to a binary Al-Cu alloy to study the interfacial characteristics for a range of growth velocities. The developed model can be used to study the effect of an applied thermal gradient, steady-state interface velocity, cell width and initial composition on the existence of cellular/dendritic structures.

The results from the cell model include the shape of the solid-liquid interface, the position of the tip with respect to the liquidus isotherm and the concentration profile in the liquid phase. The steady-state concentration profile and shape of the interface obtained using the cell model for tip velocity $V = 1.0\,\mathrm{cm\,s^{-1}}$ and cell spacing $W = 0.10\,\mu\mathrm{m}$ is shown in Figure 5.1. In the model, no diffusion was considered in the solid phase, and the solid dark blue colour in the Figure 5.1 represents the solid phase. Moreover, the cell tip was located approximately $9.28\,\mu\mathrm{m}$ behind the liquidus isotherm. As mentioned previously in Chapter 4, the liquidus isotherm was arbitrarily set at the origin and the position of the tip in the temperature field was a variable that was identified using the cell model. In addition to this, complete mixing can be

seen in the inter-dendritic region at the base of the tip. Moreover, the composition profile only varies in the z-direction at a far enough distance from the tip as seen in Figure 5.1.

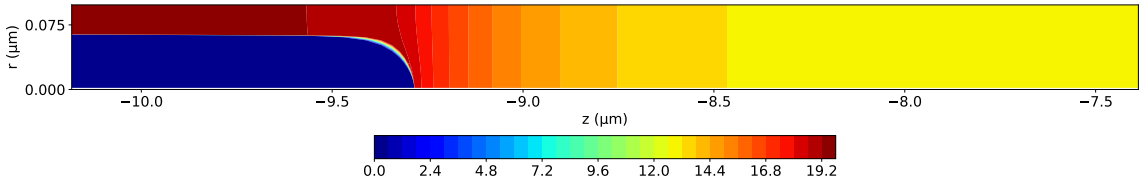

Figure 5.1: Concentration profile in the liquid phase and the shape of the interface obtained using the cell model for $V = 1.0\,\mathrm{cm\,s^{-1}}$ and $W = 0.10\,\mu\mathrm{m}$. The solid region in dark blue colour is the solid phase which is not modelled in the present work.

The solutions were iterated until the error in the composition profile obtained using the Eq. 4.3.1 and Eq. 4.3.3 was less than 10^{-7} in every CV and the error in the temperature obtained using the undercooling Eq. 4.6.3 was also than 10^{-7} at every interface grid point. A plot of the error in the temperature values at the interface grid points is shown in Figure 5.2. The error in the temperature value at every grid point was less than 10^{-7} as shown in Figure 5.2. Similarly, the error in the concentration value at each CV was also less than 10^{-7} at the time of convergence as shown in Figure 5.3.

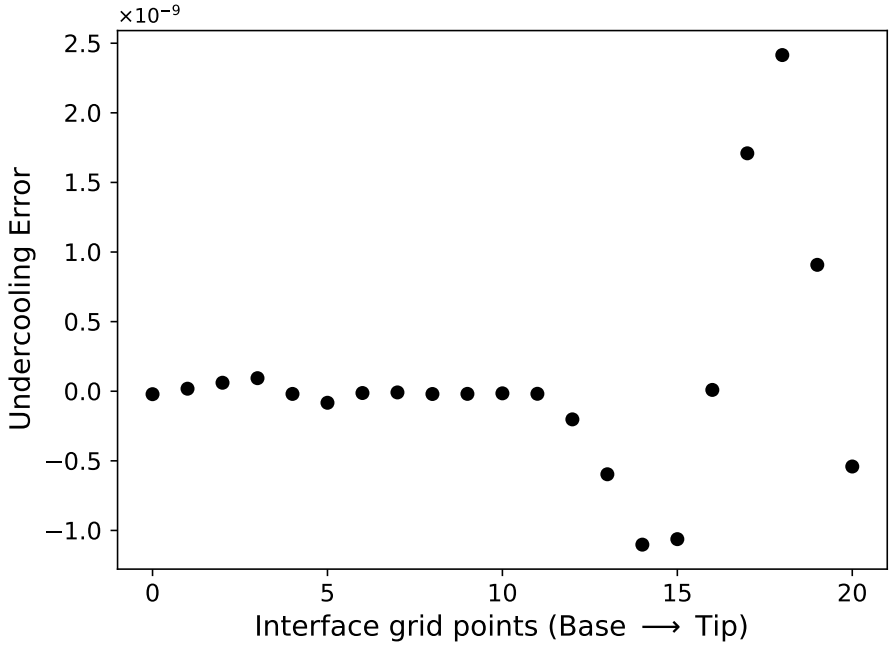

Figure 5.2: Error in the temperature obtained using the Eq. 4.6.3 at the interface grid points. The numbers on the x-axis corresponds to the interface grid points where 0 represent the base and 20 represent the tip.

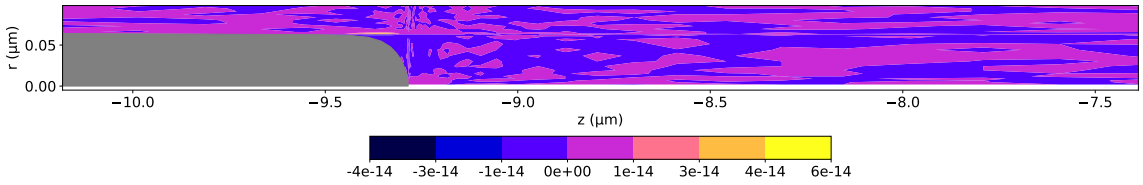

Figure 5.3: Error in the concentration profile obtained using the Eq. 4.3.1 and Eq. 4.3.3 at every CV.

5.1 Effect of Grid Size and Domain Size

In this section, the effect of grid size and domain size on the numerical results is reported. Firstly, the effect of different grid sizes on the self-consistent interface shape

and the concentration profile is analyzed. Following this, the effect of the domain size on the results obtained using the cell model is considered.

5.1.1 Effect of Grid Size

To analyze the effect of grid size on the accuracy of the numerical results, three different grid sizes were considered i.e., coarse, medium and fine grid. The parameters used for generating different grids are listed in Table 5.1. The simulations were carried out for $V = 0.1\,\mathrm{cm\,s^{-1}}$ and the results were compared at three different cell spacings $W = \{0.080,\ 0.50,\ 3.00\}$ µm. The effect of different grids on the shape of the solid-liquid interface is shown in Figure 5.4. No appreciable difference in the shape of the interface can be seen for the three different grid sizes considered in this study as shown in Figure 5.4.

Table 5.1: Parameters used for generating the grid.

	m	n	k
coarse	10	20	5
medium	20	40	10
fine	30	60	15

Next, the effect of grid size on the interface concentration and interface undercooling was considered and the results are shown in Figure 5.5 and Figure 5.6. For all different cell spacing W considered, the coarse grain failed to accurately predict the interfacial concentration and undercooling values, whereas, the composition and undercooling values almost overlap each other for the medium and fine grid as shown in Figure 5.5 and Figure 5.6 respectively. For cell spacing of 0.50 µm and 3.00 µm, the predicted interfacial concentration and interfacial undercooling are almost similar for the medium and fine grid. However, some differences in these values exist for the

medium and fine grid at 0.080 µm cell spacing.

Since no appreciable difference in the interface shape, concentration and undercooling were observed for the medium and fine grid, thus the medium grid was used for all the simulations in the remainder of this study. That usually corresponded to $m = 20$ grid points along the interface, $n = 40$ grid points ahead of the interface and $k = 10$ grid points above the interface.

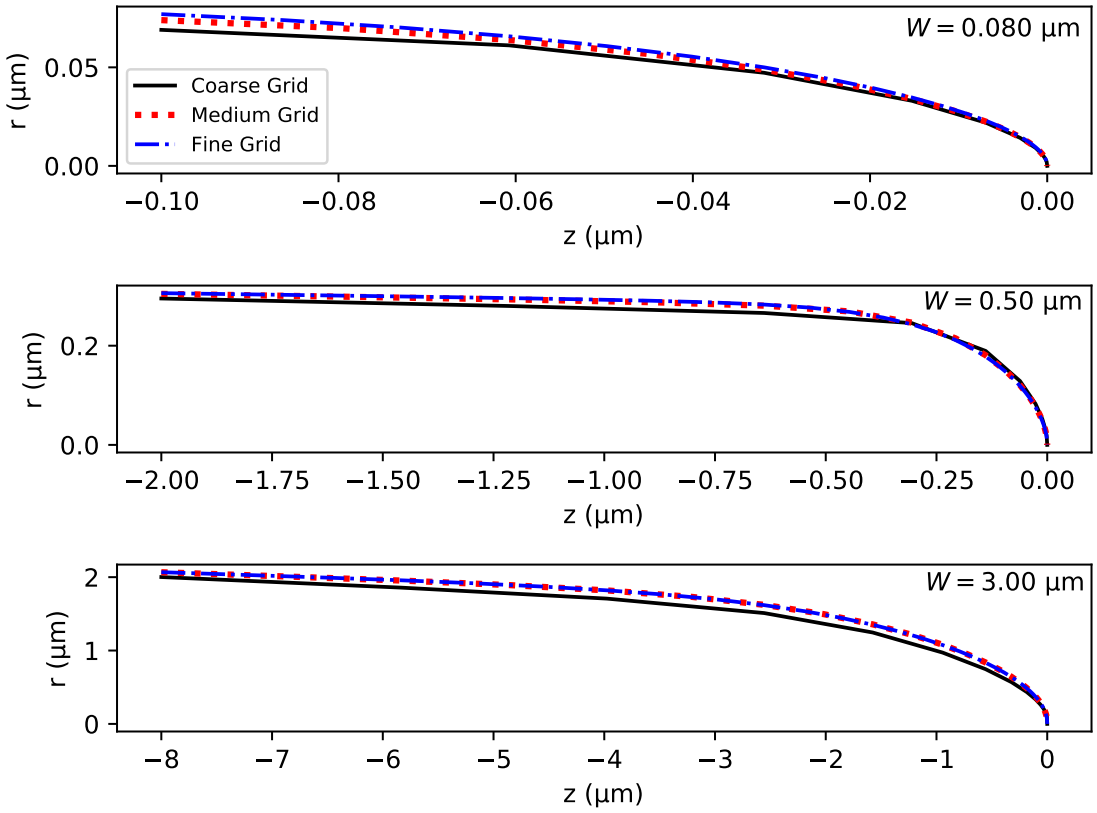

Figure 5.4: Effect of a coarse, medium and fine grid on the shape of the interface obtained using the cell model for $V = 0.1\,\mathrm{cm\,s^{-1}}$. The simulations were run for three different cell spacing W. Please note that the tip has been moved to the origin.

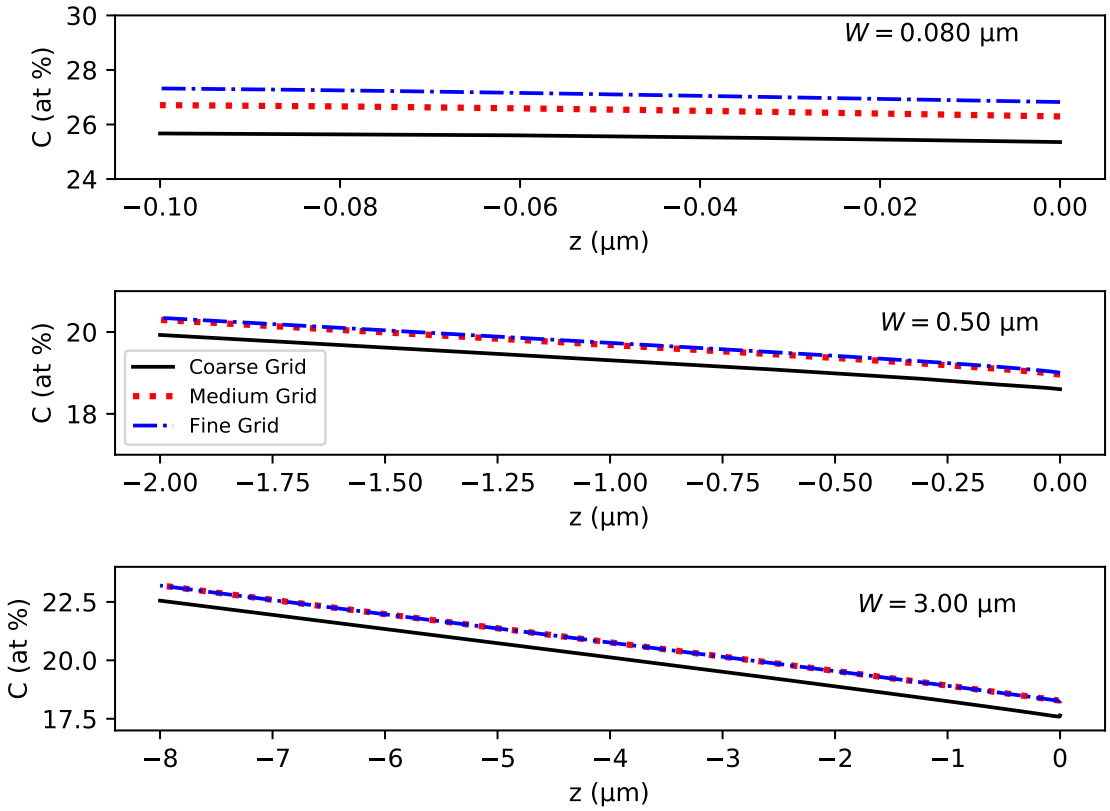

Figure 5.5: Effect of a coarse, medium and fine grid on the interfacial concentration for $V = 0.1\,\mathrm{cm\,s^{-1}}$. Please note that the tip has been moved to the origin.

5.1.2 Effect of Domain Size

In this subsection, the effect of the domain size on the interface shape, concentration and undercooling value is considered. For this purpose, the domain length L_1 and L_2 were independently varied and the resulting interfacial values were compared. The simulations were carried out at $V = 0.5\,\mathrm{cm\,s^{-1}}$ and $W = 0.50\,\mu\mathrm{m}$ using the fine grid. The numerical experiments were carried out for four different pairs of (L_1, L_2) and their values are listed in Table 5.2. As seen in the Figure 5.7 and Figure 5.8 the interfacial concentration and undercooling values were not sensitive to the domain

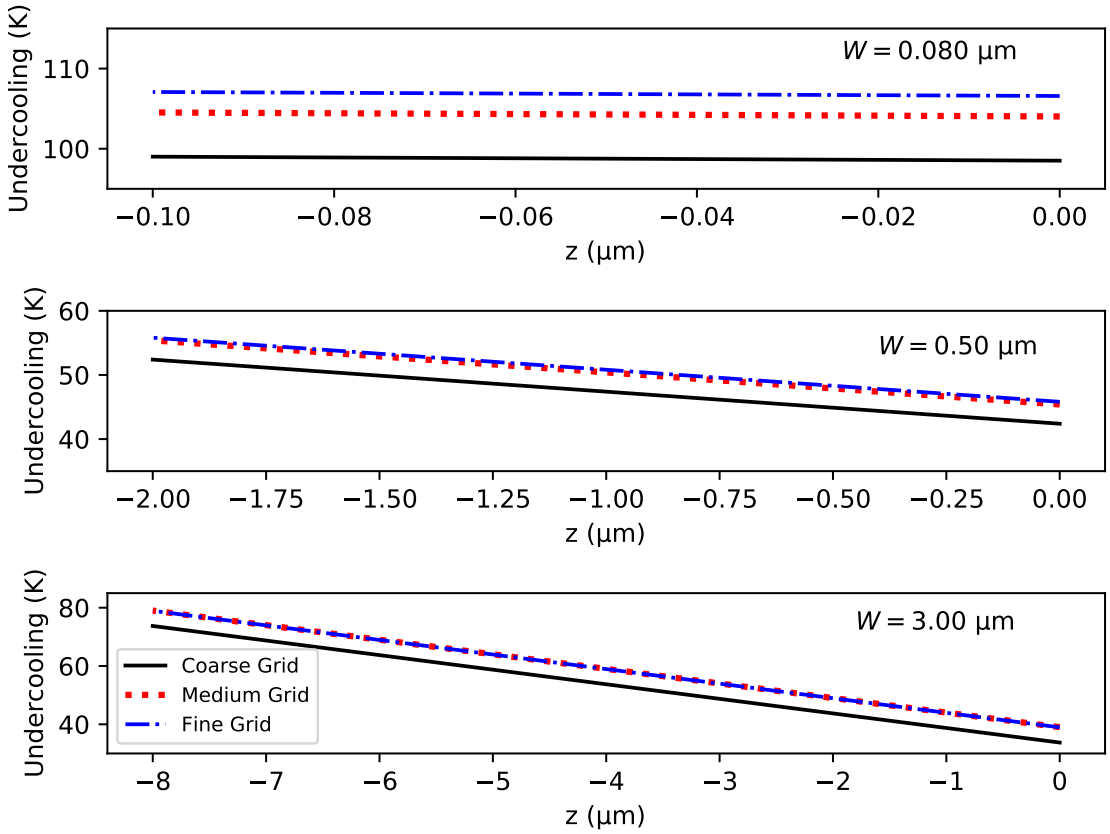

Figure 5.6: Effect of a coarse, medium and fine grid on the interface undercooling for $V = 0.1\,\mathrm{cm\,s^{-1}}$. Please note that the tip has been moved to the origin.

size as long as the L_1 and L_2 satisfied the conditions mentioned in the Section 4.2.

Table 5.2: Values of L_1 and L_2 used for analyzing the effect of domain size on the numerical results.

#	L_1 (µm)	L_2 (µm)
1	1	4
2	2	4
3	1	8
4	2	8

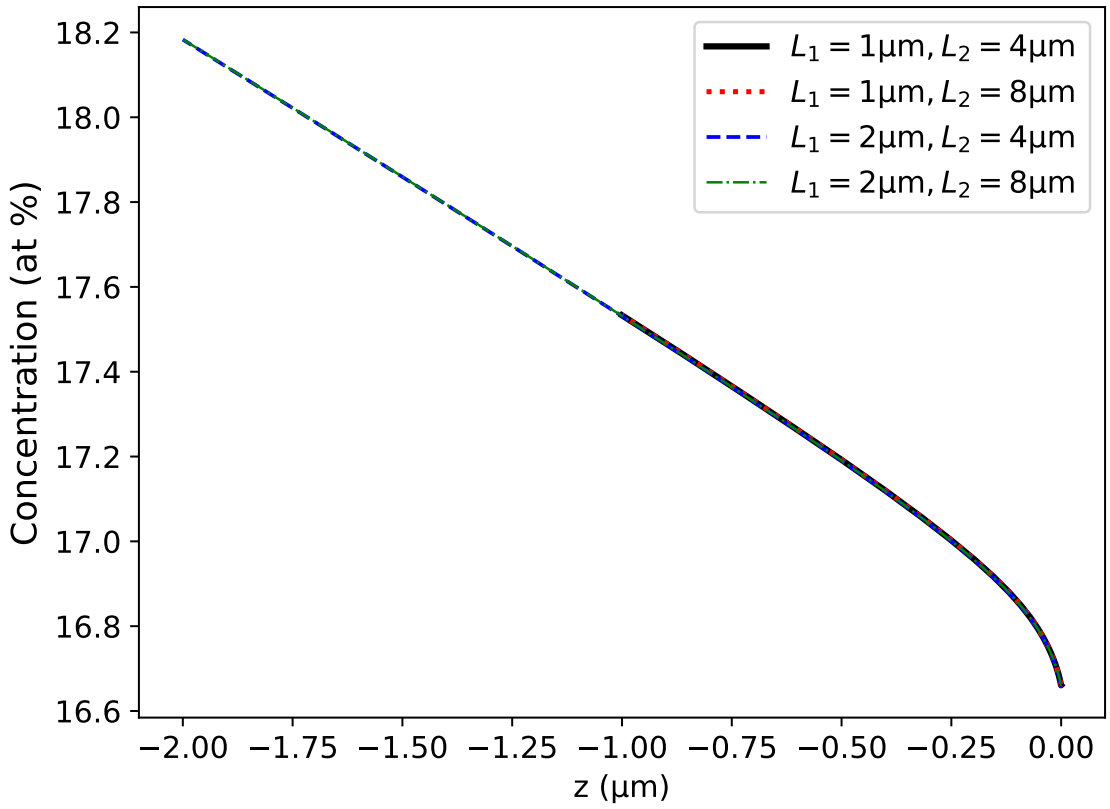

Figure 5.7: Effect of domain size on the interfacial concentration for $V = 0.5\,\mathrm{cm\,s^{-1}}$. Please note that the tip has been moved to the origin.

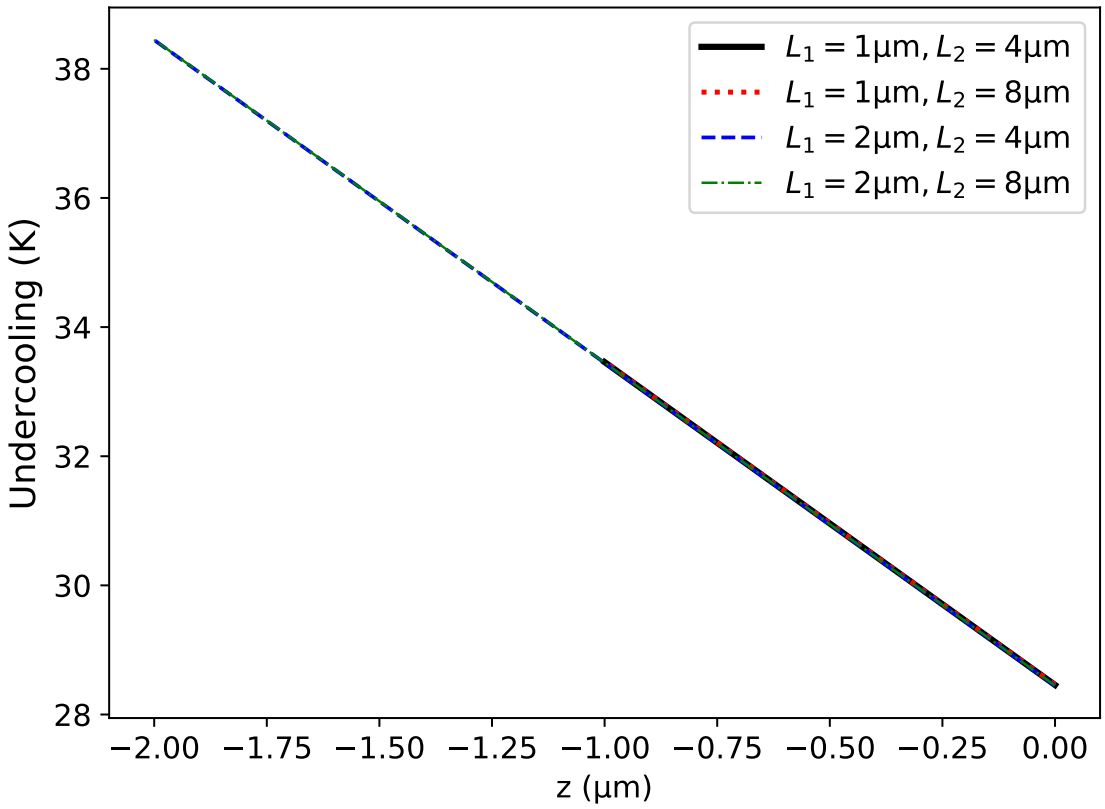

Figure 5.8: Effect of domain size on the interface undercooling for $V = 0.5\,\mathrm{cm\,s^{-1}}$. Please note that the tip has been moved to the origin.

5.2 Effect of Cell Spacing

In the cell model, the cell spacing W is a parameter that can be varied to analyze the effect of the primary spacing λ_1 on the existence of cellular/dendritic solution for a given set of input parameters. In this section, the effect of cell spacing on the shape of the solid-liquid interface, tip composition, tip radius and tip undercooling has been analyzed and presented.

Figure 5.9 shows the change in the shape of the self-consistent solid-liquid interface

obtained using the cell model as the cell spacing W was increased from 0.15 µm to 1.0 µm. At the lower spacings considered, the shape of the solid-liquid interface was characteristic of cellular structures and appear like high amplitude cells. Whereas, those obtained for larger spacing resemble more like parabolic dendrites. Please note that the smallest spacing corresponds to maximum interaction among the neighbouring cells, whereas, as the spacing increases less and less interaction will take place among the neighbouring cells with very wide spacing essentially corresponding to an isolated case. Also, note that no attempt has been made in this work to qualitatively characterize the interface shape as cellular or dendritic based on their appearance.

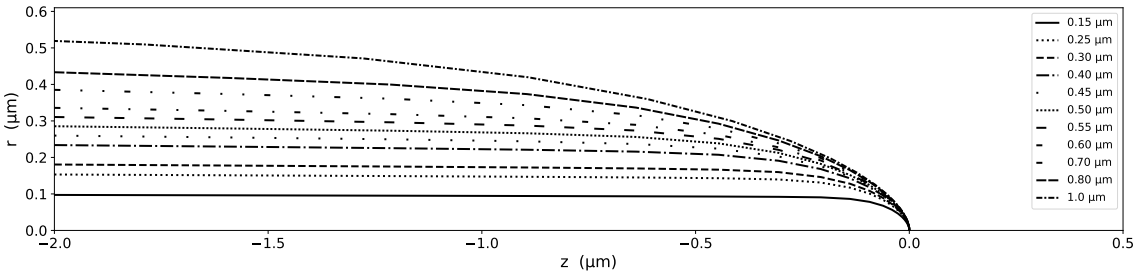

Figure 5.9: Effect of cell spacing W on the shape of the solid-liquid interface. The simulation was carried out at $V = 0.5\,\mathrm{cm\,s^{-1}}$. Please note that the interface has been plotted only up to 2 µm behind the tip and the tip has been moved to the origin.

A plot of tip composition against spacing for $V = 0.5\,\mathrm{cm\,s^{-1}}$ is shown in Figure 5.10. The tip composition had an inverse relationship with the cell spacing and as the cell spacing increased tip composition went down. At small spacings, the interaction among the solute field of the neighbouring cells will be more. Increased interaction among the neighbouring cells can make it difficult for the solute atoms to diffuse in the lateral direction which can result in an increased build-up of the solute atoms along the interface. The variation of the tip radius R with the cell spacing is shown in Figure 5.11 and the tip radius increased with the cell spacing. At low cell

spacings, very fine cellular/dendritic structures were formed with high tip curvature, whereas, as the cell spacing increased cellular/dendritic tip become broader and the tip curvature decreased as shown in Figure 5.9.

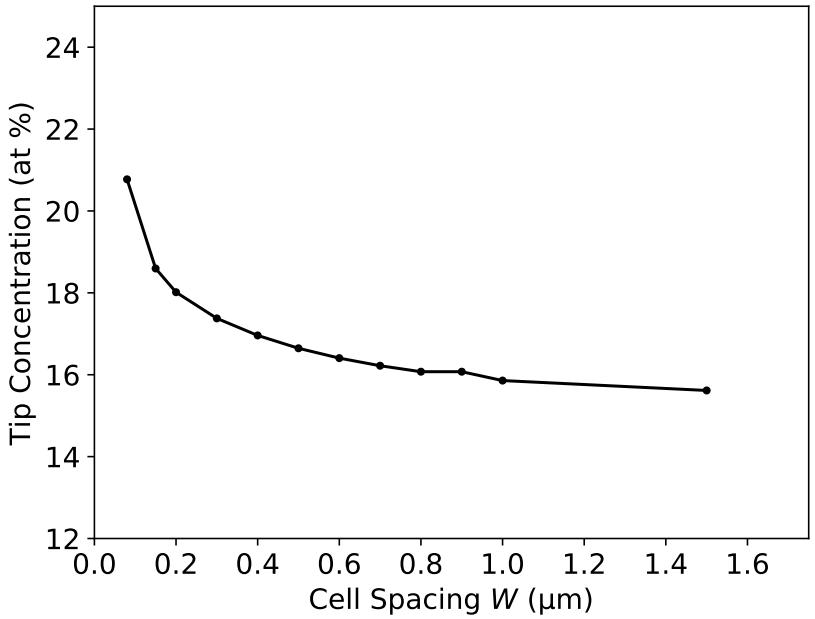

Figure 5.10: Effect of cell spacing W on tip composition for $V = 0.5\,\mathrm{cm\,s^{-1}}$.

Finally, the effect of cell spacing on the tip undercooling can be seen in Figure 5.12. The tip undercooling also had an inverse relationship with the cell spacing. The increase in the tip undercooling at lower spacing could be seen as a combined effect of the constitutional and curvature undercooling. However, the contribution of the curvature undercooling was negligible in comparison to constitutional undercooling and the increase in tip undercooling was mainly due to the constitutional undercooling.

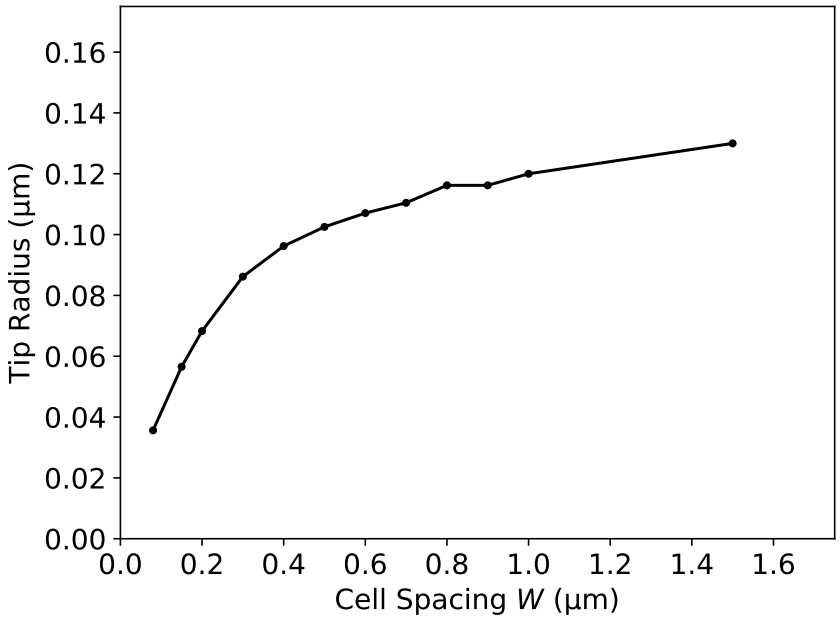

Figure 5.11: Effect of cell spacing W on tip radius for $V = 0.5\,\mathrm{cm\,s^{-1}}$.

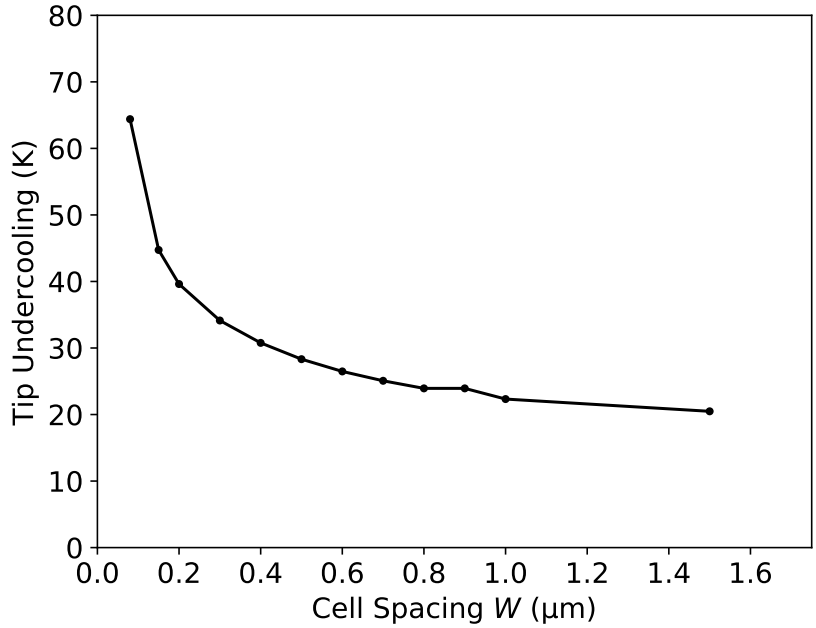

Figure 5.12: Effect of cell spacing W on tip undercooling for $V = 0.5\,\mathrm{cm\,s^{-1}}$.

5.3 Primary Spacing, Tip Composition, Radius and Undercooling

In this section, the cell model is applied to identify the range of cell/primary spacing for which a self-consistent solid-liquid interface exists at a given interface velocity. Following this, the variation of the tip composition, tip radius and tip undercooling against the interface velocity and cell spacing has also been considered in this section.

5.3.1 Primary Spacing

Figure 5.13 shows the range of primary spacing $\lambda_1 = 2W$ for which self-consistent interface shapes were identified in the present study. The numerical spacing was also compared with the spacing values predicted by the KGT model [60] and the experimental spacing from the laser resolidification experiment [3].

To find the range of cell spacing at which self-consistent solutions exists at a given growth condition, the cell spacing W was scanned to find the minimum and maximum spacing limit. In the Figure 5.13 the squares represent the smallest spacing, whereas the diamonds represent the largest spacing at which the model converged to a solution. The grey area between the upper (diamonds) and lower (squares) limit represents intermediate spacing at which convergent solutions also exist. Please note that there exists an upper critical spacing beyond which the cells/dendrites will be unstable. Above this critical limit, the cellular/dendritic spacing will adjust through tip splitting in the case of cells and tertiary arm growth in the case of dendrites. Similarly, a lower critical spacing limit also exists. Beyond the lower limit, the cells/dendrites will be subjected to an overgrowth mechanism. These phenomena ensures that in practice

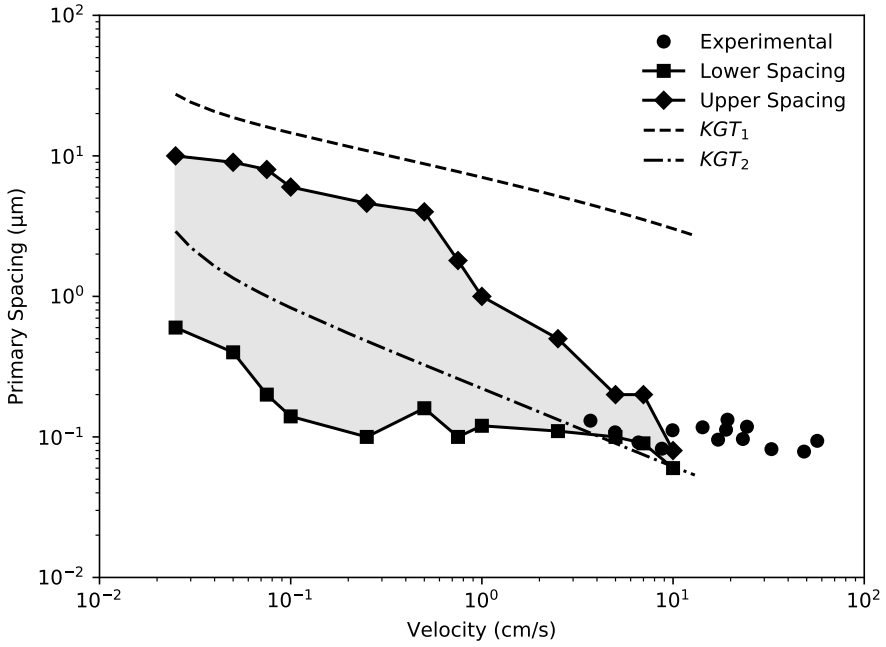

Figure 5.13: The range of primary spacing ($2W$) for which self-consistent interface shapes were identified is plotted against velocity. The square and diamonds correspond to the minimum and the maximum primary spacing, and the grey area corresponds to the intermediate spacing at which self-consistent interface shapes were identified. For comparison, the primary spacing calculated using the KGT model is also plotted. Two different approaches were used to identify the primary spacing using the KGT model referred to as KGT_1 and KGT_2. The circles correspond to the experimental spacings obtained from the laser resolidification experiments [3].

the cells/dendrites grow within a small stable spacing range [2]. Also note that in the present work, no stability analysis has been done to figure out the stable spacing range in Figure 5.13.

To compare the numerical spacing with the spacing value predicted using the KGT model, two different approaches were considered in the present work. In the first approach KGT_1, to calculate the primary spacing λ_1 an array of dendritic envelope similar to Figure 4.1a was considered where the tip dynamics was given by the KGT

model [21] and the primary spacing can be expressed as

$$\lambda_1 = \left(\frac{4\Delta T_0^v R}{G} \right)^{1/2}, \tag{5.3.1}$$

where R was calculated using the KGT model. In the second approach KGT_2, the primary spacing was assumed to be twice the KGT tip radius. The primary spacing predicted using the two approaches is plotted in Figure 5.13. The primary spacing predicted using the second approach KGT_2 was within the spacing range found using the cell model.

The primary spacing measurements from the laser resolidification experiment has also been plotted in the Figure 5.13. A good agreement exists between the experimental and the numerical spacing as shown in the figure. However, at the present moment, the numerical model is not able to go beyond the velocity of $10\,\mathrm{cm\,s^{-1}}$. The sensitivity of Newton's method to the initial guess is believed to be the reason behind the instability of the model at high velocities, and continual efforts are underway to improve the model so that it can be applied to even higher velocities.

5.3.2 Tip Composition, Radius and Undercooling

The variation of the tip composition and the tip radius against velocity is plotted in Figure 5.14 and Figure 5.15 respectively, along with the corresponding values obtained via the KGT model. The squares and diamonds correspond to the composition and radius values calculated at the lower and upper spacing limit which were identified in Figure 5.13.

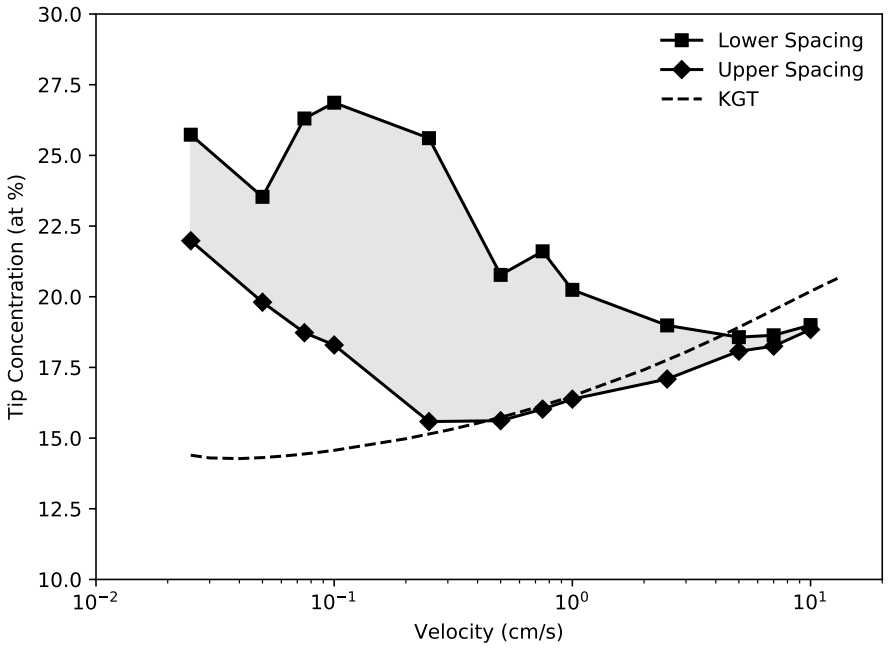

Figure 5.14: Tip composition against growth velocity for a range of primary spacing identified in Figure 5.13. For comparison the tip composition obtained using the KGT model is also plotted.

As seen in the Figure 5.14, the KGT composition was in good agreement with the numerical composition at the upper spacing limit for high growth velocities. However, significant deviation exists between the two at low growth velocities. A poor match at low growth velocities is thought to have occurred because of the interaction between the neighbouring cells, whereas, at high growth velocities little solutal interaction will take place between the adjacent cells since the spacing Péclet number was approaching 1 as shown in Figure 5.17. This situation better corresponds with the KGT model assumption of an isolated dendrite. At low growth velocities, the ability of the cell model to take into consideration the solutal interaction between the neighbouring cells leads to higher tip concentration. The same can be seen in the case of the tip

radius also. The KGT tip radius was close to the predicted upper spacing tip radius at high growth velocities where the interaction between the neighbouring cells was less compared to lower spacing.

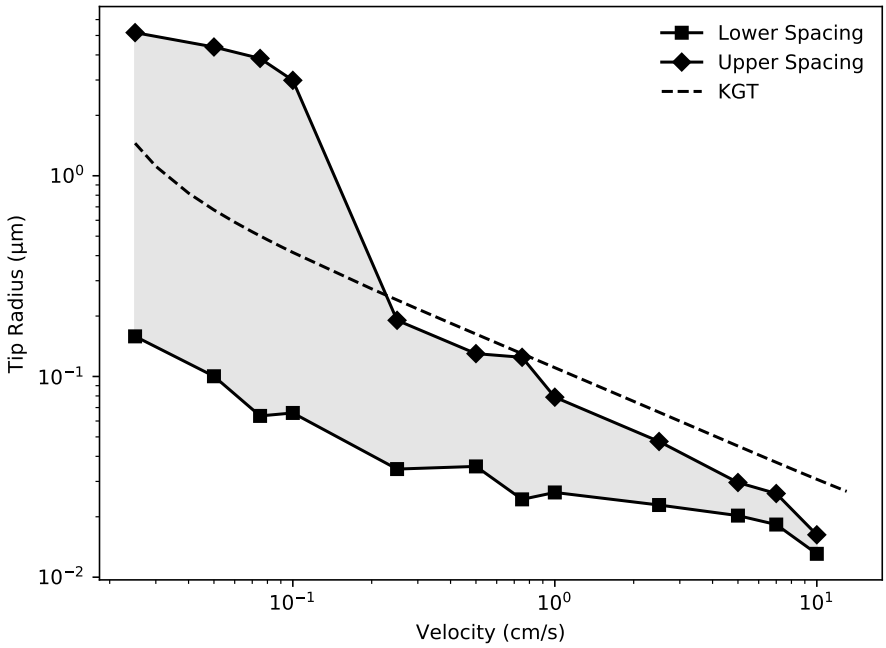

Figure 5.15: Tip radius plotted against growth velocity for a range of primary spacing identified in Figure 5.13. The KGT tip radius is also plotted in the figure.

The variation of the tip undercooling against tip velocity is plotted in Figure 5.16. The individual contribution of the constitutional and curvature undercooling to the total tip undercooling is also shown in the Figure 5.16. As can be seen, the tip undercooling decreased with increasing cell spacing. This is due to the increased solutal interaction at lower spacings which leads to solute build along the interface and thus higher constitutional undercooling. Moreover, most of the driving force for the solidification came from the constitutional undercooling and the contribution of the curvature undercooling was only significant at high growth velocities.

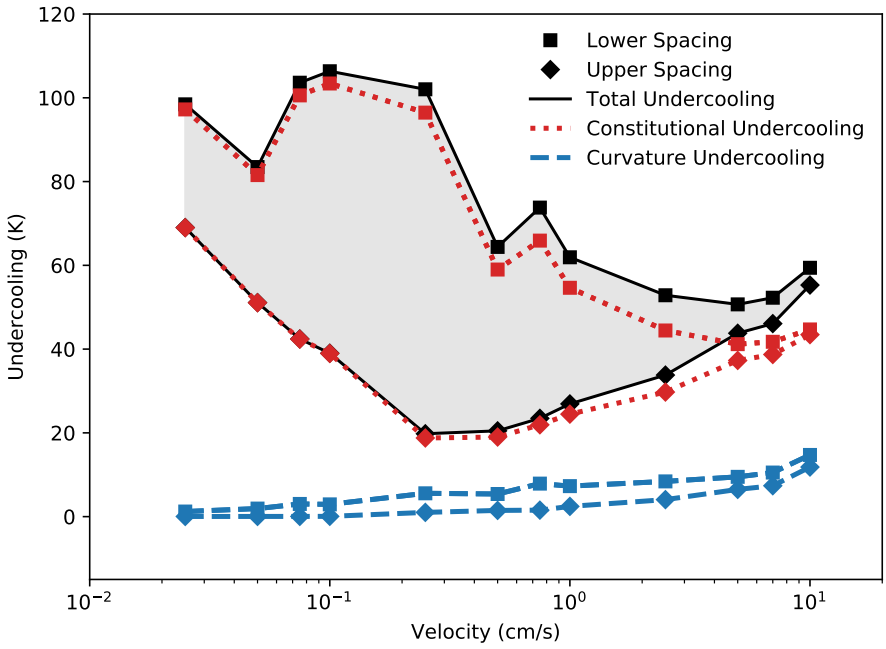

Figure 5.16: A Plot of the total tip undercooling along with the individual contribution of the constitutional and curvature undercooling against growth velocity for the spacing limit shown in Figure 5.13.

5.4 Tip and Spacing Péclet Number

In this section, the variation of the tip (top) and spacing (bottom) Péclet number for a range of growth velocity is shown in Figure 5.17. In addition to this, the variation of the Péclet number with cell spacing at a given velocity has also been shown in the Figure 5.17. Péclet number is an important dimensionless parameter which is defined as the ratio of the microstructural length scale and the diffusion length scales. At low growth velocities, this ratio is much less than 1, whereas, at high growth velocities the two length scales are of similar order and the Péclet number tends to be 1 or greater. When the microstructural and diffusion length scales are of a similar order, the classical growth theories cannot be used to model the solidification

process.

The tip Péclet number was less than 0.5 for the complete range of growth velocity as shown in Figure 5.17 (top). Moreover, the tip Péclet number increased with the growth velocity which points towards the localization of the diffusion field near the tip region at high growth velocities. Please note that the high tip Péclet number predicted for the upper spacing limit at low growth velocities was due to the large value of tip radius as shown in Figure 5.15. However, as mentioned previously the cells/dendrites are expected to be unstable at that cell spacing and therefore in practice such high tip Péclet number are unlikely.

Figure 5.17 (bottom) shows the variation of the spacing Péclet number against velocity which is an important dimensionless parameter for cellular structures. At the lower spacing limit, the spacing Péclet number was smoothly increasing with the growth velocity that approached 1 at high growth velocities. Relatively high spacing Péclet number was predicted for upper spacing limit even at low velocities. However, as mentioned previously the cellular/dendritic structures are likely to be unstable at those spacings values and therefore such high Péclet numbers are not expected to exist in practice. Also, note that the abrupt increase in the spacing Péclet number at medium growth velocity at upper spacing limit is a numerical artefact since self-consistent solutions have been found at those primary spacings. A good agreement between the numerical model and the KGT model was found at high growth velocities since much less interaction takes place among the neighbouring cells at high Péclet numbers. Moreover, at high growth velocities, the spacing Péclet number was approaching 1 and this might explain the suppressed secondary and tertiary arms as seen in experimental micrographs [148].

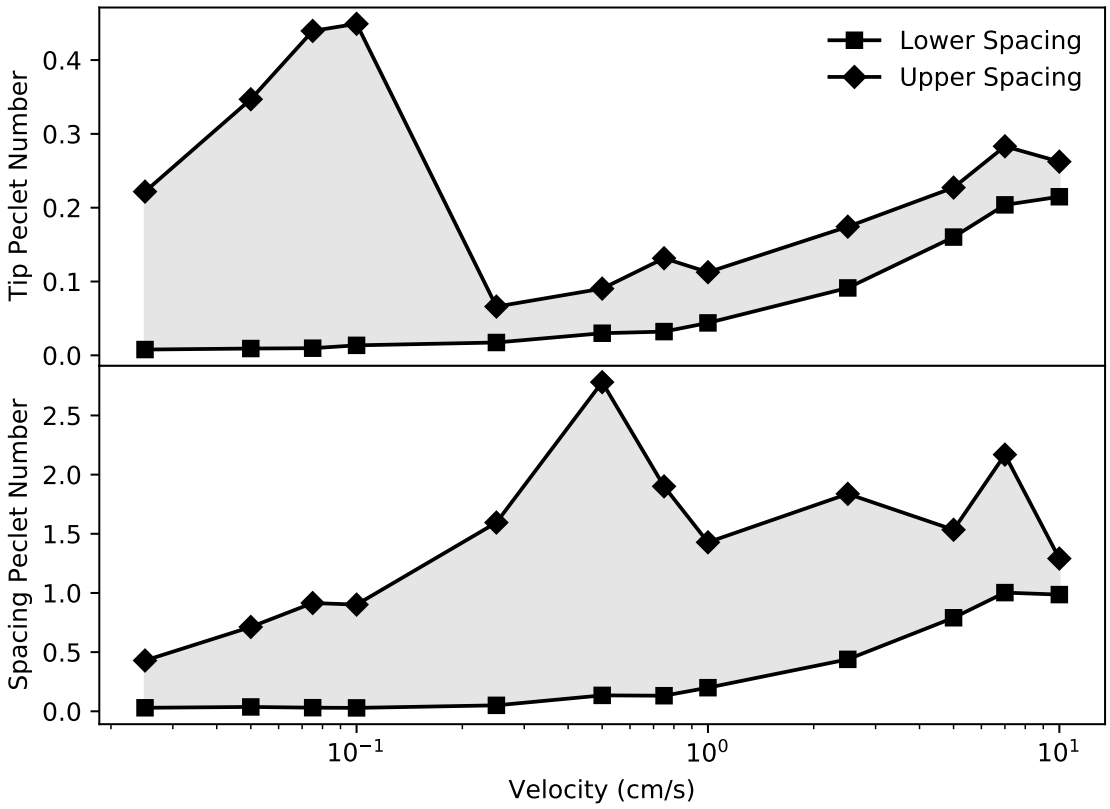

Figure 5.17: A plot of the tip Péclet number ($RV/2D_l$) and Spacing Péclet number ($\lambda_1 V/2D_l$) against growth velocity for the spacing range shown in Figure 5.13.

5.5 Sources of Uncertainty and Error; Computational Efficiency

In the cell model, the cell spacing W is a parameter and the solutions only exist for a range of cell spacing at any given set of input parameters. The numerical model proved to be very stable at the intermediate spacing range, however, the convergence was difficult at the end of the spacing range. Moreover, the solutions were sensitive to the domain length at very low and high cell spacing and a certain amount of trial

and error was required to identify the right domain size.

Similarly, the numerical model was very stable at intermediate growth velocities and easily converged to a solution. However, at very low and high growth velocities, it was difficult to find convergent solutions as evident from the Figure 5.13.

The complete mixing approximation at the left wall Γ_5 is justifiable for narrow cells, however, at large spacings, this assumption is less valid. A more appropriate boundary condition at Γ_5 can be obtained by considering the concentration gradient from an analytical solution for a paraboloid of revolution [1].

The model is computationally very efficient; at intermediate growth velocities and cell spacing, the model converged to a solution in a minute or two for the medium grid size. However, to efficiently scan the solution space using the cell model, a good initial estimate of the primary spacing at which convergent solutions can exist was required. For this purpose, the primary spacing prediction from the KGT model was used to narrow down the range of cell spacing at which the cell model was applied to identify the self-consistent solutions. Please note it took almost 10 to 15 minutes to get to a converged solution at fine grid size. At the fine grid size, the cost of numerical Jacobian estimation significantly contributes to the overall time complexity of the model.

5.6 Application to PBF-L

Despite many simplifications made in the cell model to model an array of directionally grown cells/dendrites, it is a computationally efficient method to predict the primary spacing and interfacial characteristics during the PBF process. In the present work,

the cell model has been applied to Al-Cu alloy to study the variation of the interfacial conditions with the growth velocity to identify the solidification processing zone exhibited during the PBF-L process.

Different criteria exist to classify the solidification process into different processing zones and an approximate criteria based on the interfacial velocity has been proposed by Kurz and Fisher, and Stefanescu. According to Kurz and Fisher, if the interface velocity is more than $1.0\,\mathrm{cm\,s^{-1}}$ classical growth theories based on low Péclet number approximation are not valid. Similarly, Stefanescu proposed that the metastable phase diagrams should be used at velocities greater than $1.0\,\mathrm{cm\,s^{-1}}$ since metastable transformations are possible at these velocities. Further, at velocities greater than $10.0\,\mathrm{cm\,s^{-1}}$ the local interfacial equilibrium assumption breaks down and the partition coefficient starts to deviate from the equilibrium value and as the growth velocity approaches $O(\mathrm{m/s})$, solute trapping becomes important and partitionless solidification can take place [4, 149]. Although, the above criteria based on the interface velocity serves as a good reference for classifying the solidification process into different processing zones. However, the interfacial conditions during solidification not only depend on the processing conditions but also the material system. Thus interfacial conditions such as undercooling can vary depending upon processing conditions and the material system.

Alternatively, the solidification process can be classified on the basis of the Péclet number of the corresponding microstructural feature. Accordingly, under normal solidification conditions, the Péclet number is much less than 1, whereas, rapid solidification is classified by a Péclet number of 1 or greater. In the present work, the tip Péclet number was less than 1 for the complete range of solidification velocities

considered. However, at the higher end of the interfacial velocities considered, the tip Péclet number $\sim$ 0.5, which shows the localization of the diffusion field near the tip region. Similarly, the spacing Péclet number $\approx$ 1 at the higher end of solidification velocities considered. Moreover, for the velocities considered in this study the solute trappings was not significant. The findings in this study are in agreement with the work of Boussinot et al. [148].

The variation of the composition in the semi-solid along the solid-liquid interface is shown in Figure 5.18. At low growth velocity i.e., $V = 0.1\,\mathrm{cm\,s^{-1}}$ composition varies almost linearly along the interface. This straight-line arises because the relationship between the temperature and composition given by the liquidus line is almost linear and the composition must follow the linear temperature variation in the semi-solid. However, the non-equilibrium effects at high growth velocity result in the deviation of the composition profile from a straight line as shown in Figure 5.18. Based on the results from this study, it can be said that the classical growth theories based on the low Péclet number approximation are not valid and high-velocity effects need to be considered to accurately model the solidification process during the PBF-L process.

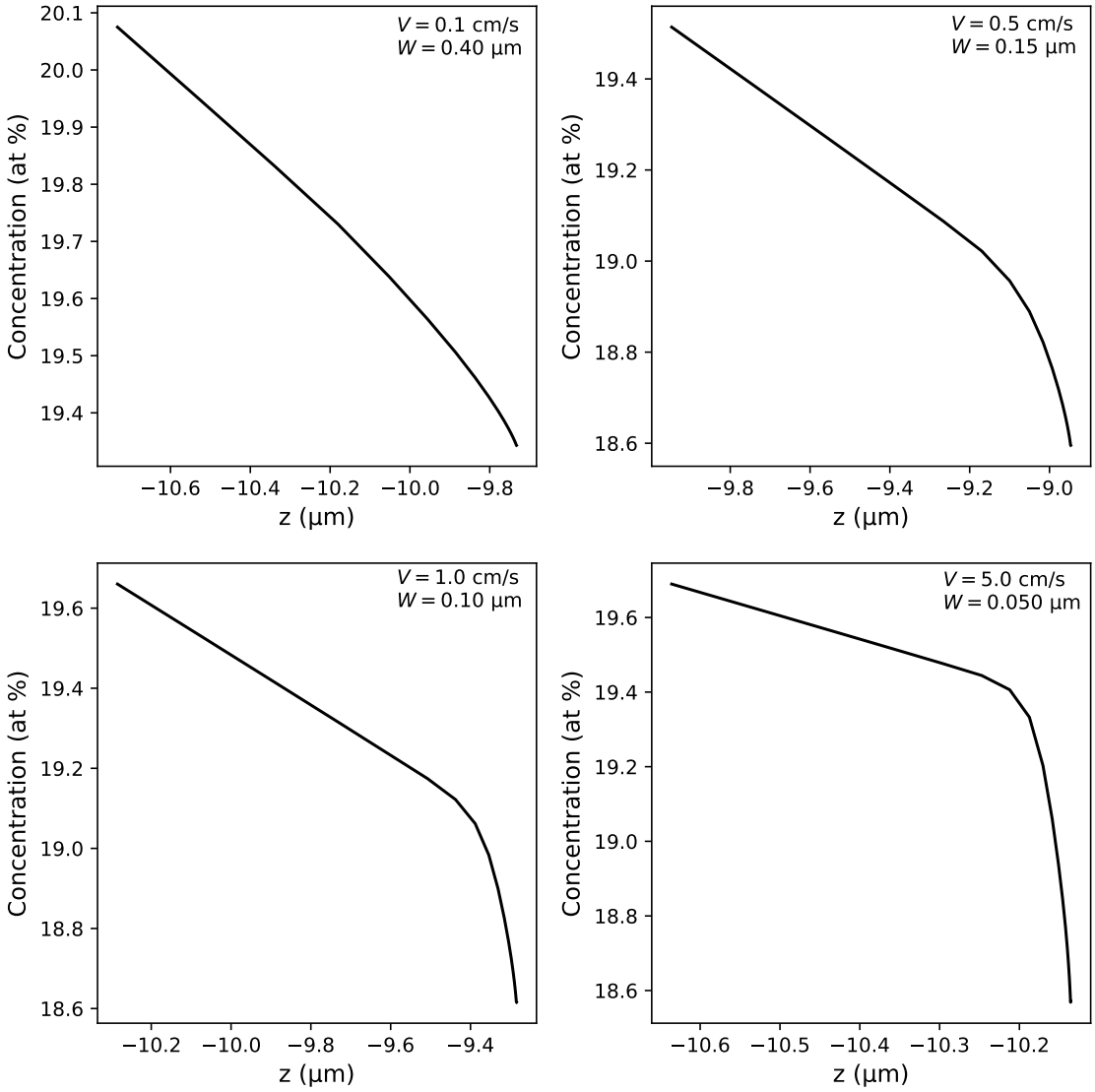

Figure 5.18: Concentration profile along the interface.

Chapter 6

Conclusions

This chapter provides key contributions of this thesis, followed by an outline of the major limitations of the present model and suggestions for future work.

6.1 Conclusions

In order to study the interfacial characteristics and identify the solidification processing zone exhibited during the PBF-L process, a numerical model was developed to simulate an array of directionally grown cells and dendrites. The developed model identifies the shape of the solid-liquid interface and the composition profile in the liquid phase for a given set of input parameters. The model is capable of simulating directional growth at both low and high interfacial velocities. At high growth velocities, the model also accounts for the non-equilibrium phenomenon by taking into consideration the variation of the partition coefficient, liquidus slope with velocity and the linear attachment kinetics. The model was used to predict the magnitude of different undercoolings along with the tip and spacing Péclet number to estimate the

extent of deviation of the solid-liquid interface from equilibrium during the PBF-L process. The key findings of the present study are as follows:

1. Self-consistent steady-state interface shapes were identified for a range of growth velocities and cell spacing.

2. The interfacial composition decreased with the increasing cell spacing. At lower spacings, the increased interaction among the neighbouring cells could lead to an increased solute built up along the interface.

3. The cell tip radius increased with increasing cell spacing.

4. Most of the driving force for the solidification came from the constitutional undercooling. The curvature undercooling was significant only at high growth velocities.

5. The model predicted the range of primary spacing at which self-consistent cellular/dendritic structures existed for a given set of input parameters. Good agreement between the numerical spacing and experimental spacing was found at high growth velocities.

6. The predicted tip composition and tip radius qualitatively agreed with the results from the KGT model. The predicted values from the numerical model and the KGT model were more in agreement at high growth velocities where the interaction among the neighbouring cells was less.

7. Moderately high tip and spacing Péclet number has been predicted at high growth velocities which shows that the non-equilibrium effects are important at high interface velocities.

6.2 Model Limitations and Potential Future Works

The critical model assumptions and the limitations of the present work are discussed along with suggestions for future work to the present study.

1. The solid-liquid interface is represented as a paraboloid of revolution and no provision exists to account for the development of secondary or tertiary arms.

2. No stability analysis has been done in the present work to identify the stable spacing range for cell and dendrites. In the future, stability analysis could be done to directly compare the predicted spacing range with the experimental data. Moreover, no distinction has been made between the cellular and dendritic structures in the present work.

3. The model is only applicable to binary alloys, however, most of the commercial PBF-L alloys have more than two components. The model could be adapted to pseudo-binary systems and further extended to multi-component alloys.

4. The model is unstable at the extremities. Convergence is difficult at the onset of constitutional undercooling and near the absolute stability region.

Bibliography

[1] J.D. Hunt. A numerical analysis of time dependent isolated dendritic growth for conditions near the steady state. *Acta Metallurgica et Materialia*, 38(3):411–418, mar 1990.

[2] Shu Zu Lu and J. D. Hunt. A numerical analysis of dendritic and cellular array growth: the spacing adjustment mechanisms. *Journal of Crystal Growth*, 123(1-2):17–34, 1992.

[3] Shu Zu Lu, J. D. Hunt, P. Gilgien, and W. Kurz. Cellular and dendritic growth in rapidly solidified AlFe and AlCu alloys. *Acta Metallurgica Et Materialia*, 42(5):1653–1660, 1994.

[4] Wilfried Kurz and David J Fisher. *Fundamentals of solidification*. Trans Tech Publ, 1989.

[5] W. Kurz. Solidification Microstructure-Processing Maps: Theory and Application. *Advanced Engineering Materials*, 3(7):443–452, jul 2001.

[6] R. Trivedi and W. Kurz. Solidification microstructures: A conceptual approach. *Acta Metallurgica Et Materialia*, 42(1):15–23, 1994.

[7] P. Mohammadpour, A. Plotkowski, and A.B. Phillion. Revisiting solidification microstructure selection maps in the frame of additive manufacturing. *Additive Manufacturing*, page 100936, 2019.

[8] WJ Boettinger, JH Perepezko, SK Das, BH Kear, and CM Adam. Rapidly solidified crystalline alloys. *Fundamentals in Rapid Solidification*, 1985.

[9] M. Carrard, M. Gremaud, M. Zimmermann, and W. Kurz. About the banded structure in rapidly solidified dendritic and eutectic alloys. *Acta Metallurgica Et Materialia*, 40(5):983–996, 1992.

[10] T. DebRoy, H. L. Wei, J. S. Zuback, T. Mukherjee, J. W. Elmer, J. O. Milewski, A. M. Beese, A. Wilson-Heid, A. De, and W. Zhang. Additive manufacturing of metallic components – Process, structure and properties. *Progress in Materials Science*, 92:112–224, 2018.

[11] Dirk Herzog, Vanessa Seyda, Eric Wycisk, and Claus Emmelmann. Additive manufacturing of metals. *Acta Materialia*, 117:371–392, 2016.

[12] Kaufui V. Wong and Aldo Hernandez. A Review of Additive Manufacturing. *ISRN Mechanical Engineering*, 2012:1–10, 2012.

[13] W. J. Sames, F. A. List, S. Pannala, R. R. Dehoff, and S. S. Babu. The metallurgy and processing science of metal additive manufacturing. *International Materials Reviews*, 61(5):315–360, 2016.

[14] Samuel H. Huang, Peng Liu, Abhiram Mokasdar, and Liang Hou. Additive manufacturing and its societal impact: A literature review. *International Journal of Advanced Manufacturing Technology*, 67(5-8):1191–1203, 2013.

[15] Jian Yuan Lee, Jia An, and Chee Kai Chua. Fundamentals and applications of 3D printing for novel materials. *Applied Materials Today*, 7:120–133, 2017.

[16] Claus Emmelmann, Jannis Kranz, Dirk Herzog, and Eric Wycisk. Laser additive manufacturing of metals. In *Laser technology in biomimetics*, pages 143–162. Springer, 2013.

[17] William E. Frazier. Metal additive manufacturing: A review. *Journal of Materials Engineering and Performance*, 23(6):1917–1928, 2014.

[18] Tuan D. Ngo, Alireza Kashani, Gabriele Imbalzano, Kate T.Q. Nguyen, and David Hui. Additive manufacturing (3D printing): A review of materials, methods, applications and challenges. *Composites Part B: Engineering*, 143(February):172–196, 2018.

[19] Patcharapit Promoppatum, Shi Chune Yao, P. Chris Pistorius, and Anthony D. Rollett. A Comprehensive Comparison of the Analytical and Numerical Prediction of the Thermal History and Solidification Microstructure of Inconel 718 Products Made by Laser Powder-Bed Fusion. *Engineering*, 3(5):685–694, 2017.

[20] Stephen H Davis. *Theory of solidification*. Cambridge University Press, 2001.

[21] Jonathan A Dantzig and Michel Rappaz. *Solidification: -Revised & Expanded*. EPFL press, 2016.

[22] W. Kurz and R. Trivedi. Overview no. 87 solidification microstructures: Recent developments and future directions. *Acta Metallurgica et Materialia*, 38(1):1–17, Jan 1990.

[23] Biswajit Basu and A. W. Date. Numerical modelling of melting and solidification problems-A review. *Sadhana*, 13(3):169–213, 1988.

[24] David A Porter and Kenneth E Easterling. *Phase transformations in metals and alloys (revised reprint)*. CRC press, 2009.

[25] Merton C Flemings. Solidification processing. *Metallurgical transactions*, 5(10):2121–2134, 1974.

[26] M. J. Aziz. Model for solute redistribution during rapid solidification. *Journal of Applied Physics*, 53(2):1158–1168, 1982.

[27] YP Hu, CW Chen, and K Mukherjee. Measurement of temperature distributions during laser cladding process. *Journal of Laser Applications*, 12(3):126–130, 2000.

[28] Tarak Amine, Joseph W Newkirk, and Frank Liou. Investigation of effect of process parameters on multilayer builds by direct metal deposition. *Applied thermal engineering*, 73(1):500–511, 2014.

[29] Steven Price, Ken Cooper, and Kevin Chou. Evaluations of temperature measurements by near-infrared thermography in powder-based electron-beam additive manufacturing. In *Proceedings of the Solid Freeform Fabrication Symposium*, pages 761–773. University of Texas, Austin, TX, 2012.

[30] Paul A. Hooper. Melt pool temperature and cooling rates in laser powder bed fusion. *Additive Manufacturing*, 22(May):548–559, 2018.

[31] Umberto Scipioni Bertoli, Gabe Guss, Sheldon Wu, Manyalibo J. Matthews, and Julie M. Schoenung. In-situ characterization of laser-powder interaction

and cooling rates through high-speed imaging of powder bed fusion additive manufacturing. *Materials and Design*, 135:385–396, 2017.

[32] Cang Zhao, Kamel Fezzaa, Ross W. Cunningham, Haidan Wen, Francesco De Carlo, Lianyi Chen, Anthony D. Rollett, and Tao Sun. Real-time monitoring of laser powder bed fusion process using high-speed X-ray imaging and diffraction. *Scientific Reports*, 7(1):1–11, 2017.

[33] M. M. Francois, A. Sun, W. E. King, N. J. Henson, D. Tourret, C. A. Bronkhorst, N. N. Carlson, C. K. Newman, T. Haut, J. Bakosi, J. W. Gibbs, V. Livescu, S. A. Vander Wiel, A. J. Clarke, M. W. Schraad, T. Blacker, H. Lim, T. Rodgers, S. Owen, F. Abdeljawad, J. Madison, A. T. Anderson, J. L. Fattebert, R. M. Ferencz, N. E. Hodge, S. A. Khairallah, and O. Walton. Modeling of additive manufacturing processes for metals: Challenges and opportunities. *Current Opinion in Solid State and Materials Science*, 21(4):198–206, 2017.

[34] John G. Michopoulos, Athanasios P. Iliopoulos, John C. Steuben, Andrew J. Birnbaum, and Samuel G. Lambrakos. On the multiphysics modeling challenges for metal additive manufacturing processes. *Additive Manufacturing*, 22(February 2015):784–799, 2018.

[35] Dongdong Gu, Yves-Christian Hagedorn, Wilhelm Meiners, Guangbin Meng, Rui João Santos Batista, Konrad Wissenbach, and Reinhart Poprawe. Densification behavior, microstructure evolution, and wear performance of selective laser melting processed commercially pure titanium. *Acta Materialia*, 60(9):3849–3860, 2012.

[36] Alphons Anandaraj Antonysamy, J Meyer, and PB Prangnell. Effect of build geometry on the β-grain structure and texture in additive manufacture of ti6al4v by selective electron beam melting. *Materials characterization*, 84:153–168, 2013.

[37] Xipeng Tan, Yihong Kok, Yu Jun Tan, Marion Descoins, Dominique Mangelinck, Shu Beng Tor, Kah Fai Leong, and Chee Kai Chua. Graded microstructure and mechanical properties of additive manufactured ti–6al–4v via electron beam melting. *Acta Materialia*, 97:1–16, 2015.

[38] M Froend, V Ventzke, N Kashaev, B Klusemann, and J Enz. Thermal analysis of wire-based direct energy deposition of al-mg using different laser irradiances. *Additive Manufacturing*, 29:100800, 2019.

[39] W. Kurz and R. Trivedi. Overview No. 87 Solidification microstructures: Recent developments and future directions. *Acta Metallurgica et Materialia*, 38(1):1–17, jan 1990.

[40] Wilfried Kurz, David J. Fisher, and Rohit Trivedi. Progress in modelling solidification microstructures in metals and alloys: dendrites and cells from 1700 to 2000. *International Materials Reviews*, 64(6):311–354, 2019.

[41] William W Mullins and RF Sekerka. Stability of a planar interface during solidification of a dilute binary alloy. *Journal of applied physics*, 35(2):444–451, 1964.

[42] Przemek Kopczyński, Wouter-Jan Rappel, and Alain Karma. Critical role of

crystalline anisotropy in the stability of cellular array structures in directional solidification. *Physical review letters*, 77(16):3387, 1996.

[43] GB McFadden and SR Coriell. Nonplanar interface morphologies during unidirectional solidification of a binary alloy. *Physica D: Nonlinear Phenomena*, 12(1-3):253–261, 1984.

[44] GB McFadden, RF Boisvert, and SR Coriell. Nonplanar interface morphologies during unidirectional solidification of a binary alloy: Ii. three-dimensional computations. *Journal of crystal growth*, 84(3):371–388, 1987.

[45] MA Eshelman, V Seetharaman, and R Trivedi. Cellular spacings—i. steady-state growth. *Acta metallurgica*, 36(4):1165–1174, 1988.

[46] R Trivedi and W Kurz. Dendritic growth. *International Materials Reviews*, 39(2):49–74, jan 1994.

[47] ME Glicksman, RJ Schaefer, and JD Ayers. Dendritic growth-a test of theory. *Metallurgical Transactions A*, 7(11):1747–1759, 1976.

[48] S.-C. Huang and M.E. Glicksman. Overview 12: Fundamentals of dendritic solidification—I. Steady-state tip growth. *Acta Metallurgica*, 29(5):701–715, may 1981.

[49] JS Langer and J Müller-Krumbhaar. Stability effects in dendritic crystal growth. *Journal of Crystal Growth*, 42:11–14, 1977.

[50] JS Langer and H Müller-Krumbhaar. Theory of dendritic growth—i. elements of a stability analysis. *Acta Metallurgica*, 26(11):1681–1687, 1978.

[51] Daniel I Meiron. Selection of steady states in the two-dimensional symmetric model of dendritic growth. *Physical Review A*, 33(4):2704, 1986.

[52] P Pelce and Y Pomeau. Dendrites in the small undercooling limit. In *Dynamics of Curved Fronts*, pages 327–340. Elsevier, 1988.

[53] M Ben Amar and Y Pomeau. Theory of dendritic growth in a weakly undercooled melt. *EPL (Europhysics Letters)*, 2(4):307, 1986.

[54] Angelo Barbieri, Daniel C Hong, and JS Langer. Velocity selection in the symmetric model of dendritic crystal growth. *Physical Review A*, 35(4):1802, 1987.

[55] David A Kessler and Herbert Levine. Stability of dendritic crystals. *Physical review letters*, 57(24):3069, 1986.

[56] David Bensimon, Pierre Pelcé, and Boris I Shraiman. Dynamics of curved fronts and pattern selection. *Journal de Physique*, 48(12):2081–2087, 1987.

[57] J S Langer. Existence of needle crystals in local models of solidification. *Physical Review A*, 33(1):435–441, 1986.

[58] M Ben Amar and P Pelcé. Impurity effect on dendritic growth. *Physical Review A*, 39(8):4263–4269, 1989.

[59] R. Trivedi and W. Kurz. Morphological stability of a planar interface under rapid solidification conditions. *Acta Metallurgica*, 34(8):1663–1670, 1986.

[60] W. Kurz, B. Giovanola, and R. Trivedi. Theory of microstructural development during rapid solidification. *Acta Metallurgica*, 34(5):823–830, 1986.

[61] J Lipton, W Kurz, and R Trivedp. RAPID DENDRITE GROWTH IN UNDERCOOLED ALLOYS. *Acta metall*, 35(4):951–964, 1987.

[62] W. J. Boettinger, S. R. Coriell, A. L. Greer, A. Karma, W. Kurz, M. Rappaz, and R. Trivedi. Solidification microstructures: recent developments, future directions. *Acta Materialia*, 48(1):43–70, 2000.

[63] Amir Hadadzadeh, Babak Shalchi Amirkhiz, Jian Li, and Mohsen Mohammadi. Columnar to equiaxed transition during direct metal laser sintering of AlSi10Mg alloy: Effect of building direction. *Additive Manufacturing*, 23(June):121–131, 2018.

[64] Lore Thijs, Karolien Kempen, Jean Pierre Kruth, and Jan Van Humbeeck. Fine-structured aluminium products with controllable texture by selective laser melting of pre-alloyed AlSi10Mg powder. *Acta Materialia*, 61(5):1809–1819, 2013.

[65] Erhard Brandl, Ulrike Heckenberger, Vitus Holzinger, and Damien Buchbinder. Additive manufactured AlSi10Mg samples using Selective Laser Melting (SLM): Microstructure, high cycle fatigue, and fracture behavior. *Materials and Design*, 34:159–169, 2012.

[66] L. P. Lam, D. Q. Zhang, Z. H. Liu, and C. K. Chua. Phase analysis and microstructure characterisation of AlSi10Mg parts produced by Selective Laser Melting. *Virtual and Physical Prototyping*, 10(4):207–215, 2015.

[67] Dunyong Deng, Ru Lin Peng, Håkan Brodin, and Johan Moverare. Microstructure and mechanical properties of Inconel 718 produced by selective laser melting: Sample orientation dependence and effects of post heat treatments. *Materials Science and Engineering A*, 713(July 2017):294–306, 2018.

[68] Mohammad H. Farshidianfar, Amir Khajepour, and Adrian P. Gerlich. Effect of real-time cooling rate on microstructure in Laser Additive Manufacturing. *Journal of Materials Processing Technology*, 231:468–478, 2016.

[69] H. Rafii-Tabar. Multi-scale computational modelling of solidification phenomena. *Physics Reports*, 365(3):145–249, jul 2002.

[70] Alain Karma and Damien Tourret. Atomistic to continuum modeling of solidification microstructures. *Current Opinion in Solid State and Materials Science*, 20(1):25–36, 2016.

[71] M Rappaz. Modelling of microstructure formation in solidification processes. *International Materials Reviews*, 34(1):93–124, 1989.

[72] J. J. Hoyt, Mark Asta, and Alain Karma. Atomistic simulation methods for computing the kinetic coefficient in solid-liquid systems. *Interface Science*, 10(2-3):181–189, 2002.

[73] J. J. Hoyt, Mark Asta, and Alain Karma. Atomistic and continuum modeling of dendritic solidification. *Materials Science and Engineering R: Reports*, 41(6):121–163, 2003.

[74] JJ Hoyt, Mark Asta, and Alain Karma. Method for computing the anisotropy

of the solid-liquid interfacial free energy. *Physical review letters*, 86(24):5530, 2001.

[75] T Frolov and Y Mishin. Solid-liquid interface free energy in binary systems: Theory and atomistic calculations for the (110) cu–ag interface. *The Journal of chemical physics*, 131(5):054702, 2009.

[76] YF Gao, Y Yang, DY Sun, M Asta, and JJ Hoyt. Molecular dynamics simulations of the crystal–melt interface mobility in hcp mg and bcc fe. *Journal of crystal growth*, 312(21):3238–3242, 2010.

[77] JJ Hoyt, M Asta, and A Karma. Atomistic simulations of solute trapping and solute drag. *Solidification of Containerless Undercooled Melts*, pages 363–380, 2012.

[78] JJ Hoyt, David Olmsted, Saryu Jindal, Mark Asta, and Alain Karma. Method for computing short-range forces between solid-liquid interfaces driving grain boundary premelting. *Physical Review E*, 79(2):020601, 2009.

[79] KR Elder and Martin Grant. Modeling elastic and plastic deformations in nonequilibrium processing using phase field crystals. *Physical Review E*, 70(5):051605, 2004.

[80] KR Elder, Mark Katakowski, Mikko Haataja, and Martin Grant. Modeling elasticity in crystal growth. *Physical review letters*, 88(24):245701, 2002.

[81] A Jaatinen, CV Achim, KR Elder, and T Ala-Nissila. Thermodynamics of bcc metals in phase-field-crystal models. *Physical Review E*, 80(3):031602, 2009.

[82] William J Boettinger, James A Warren, Christoph Beckermann, and Alain Karma. Phase-field simulation of solidification. *Annual review of materials research*, 32(1):163–194, 2002.

[83] Tomorr Haxhimali, Alain Karma, Frédéric Gonzales, and Michel Rappaz. Orientation selection in dendritic evolution. *Nature materials*, 5(8):660–664, 2006.

[84] M. Rappaz. Modeling and characterization of grain structures and defects in solidification. *Current Opinion in Solid State and Materials Science*, 20(1):37–45, 2016.

[85] John M Sullivan Jr, Daniel R Lynch, and Kevin O'Neill. Finite element simulation of planar instabilities during solidification of an undercooled melt. *Journal of Computational Physics*, 69(1):81–111, 1987.

[86] A Jacot and M Rappaz. A pseudo-front tracking technique for the modelling of solidification microstructures in multi-component alloys. *Acta Materialia*, 50(8):1909–1926, 2002.

[87] Mohamad Ali Jaafar, Daniel R. Rousse, Stéphane Gibout, and Jean Pierre Bédécarrats. A review of dendritic growth during solidification: Mathematical modeling and numerical simulations. *Renewable and Sustainable Energy Reviews*, 74(March):1064–1079, 2017.

[88] William J Boettinger and James A Warren. The phase-field method: simulation of alloy dendritic solidification during recalescence. *Metallurgical and materials transactions A*, 27(3):657–669, 1996.

[89] S Chen, B Merriman, Smereka Osher, and P Smereka. A simple level set method for solving stefan problems. *Journal of Computational Physics*, 135(1):8–29, 1997.

[90] Joaquín López, Pablo Gómez, and Julio Hernández. A volume of fluid approach for crystal growth simulation. *Journal of Computational Physics*, 229(19):6663–6672, 2010.

[91] Vaughan R Voller. An enthalpy method for modeling dendritic growth in a binary alloy. *International Journal of Heat and Mass Transfer*, 51(3-4):823–834, 2008.

[92] Ingo Steinbach. Phase-field models in materials science. *Modelling and Simulation in Materials Science and Engineering*, 17(7):073001, oct 2009.

[93] Michael Greenwood, K. N. Shampur, Nana Ofori-Opoku, Tatu Pinomaa, Lei Wang, Sebastian Gurevich, and Nikolas Provatas. Quantitative 3D phase field modelling of solidification using next-generation adaptive mesh refinement. *Computational Materials Science*, 142:153–171, 2018.

[94] Ryo Kobayashi. Modeling and numerical simulations of dendritic crystal growth. *Physica D: Nonlinear Phenomena*, 63(3-4):410–423, 1993.

[95] J. A. Warren and W. J. Boettinger. Prediction of dendritic growth and microsegregation patterns in a binary alloy using the phase-field method. *Acta Metallurgica Et Materialia*, 43(2):689–703, 1995.

[96] Adam A Wheeler, William J Boettinger, and Geoffrey B McFadden. Phase-field model for isothermal phase transitions in binary alloys. *Physical Review A*, 45(10):7424, 1992.

[97] Gunduz Caginalp and Weiqing Xie. Phase-field and sharp-interface alloy models. *Physical Review E*, 48(3):1897, 1993.

[98] Seong Gyoon Kim, Won Tae Kim, and Toshio Suzuki. Phase-field model for binary alloys. *Physical review e*, 60(6):7186, 1999.

[99] GB McFadden, AA Wheeler, RJ Braun, SR Coriell, and RF Sekerka. Phase-field models for anisotropic interfaces. *Physical Review E*, 48(3):2016, 1993.

[100] Alain Karma. Phase-field formulation for quantitative modeling of alloy solidification. *Physical Review Letters*, 87(11):115701, 2001.

[101] Alain Karma and Wouter-Jan Rappel. Quantitative phase-field modeling of dendritic growth in two and three dimensions. *Physical review E*, 57(4):4323, 1998.

[102] Blas Echebarria, Roger Folch, Alain Karma, and Mathis Plapp. Quantitative phase-field model of alloy solidification. *Physical review E*, 70(6):061604, 2004.

[103] Alain Karma and Wouter-Jan Rappel. Phase-field model of dendritic sidebranching with thermal noise. *Physical review E*, 60(4):3614, 1999.

[104] N Bergeon, D Tourret, L Chen, J-M Debierre, R Guérin, A Ramirez, B Billia, A Karma, and R Trivedi. Spatiotemporal dynamics of oscillatory cellular patterns in three-dimensional directional solidification. *Physical review letters*, 110(22):226102, 2013.

[105] Sebastian Gurevich, Alain Karma, Mathis Plapp, and Rohit Trivedi. Phase-field study of three-dimensional steady-state growth shapes in directional solidification. *Physical Review E*, 81(1):011603, 2010.

[106] Ingo Steinbach, Franco Pezzolla, Britta Nestler, Markus Seeßelberg, Robert Prieler, Georg J Schmitz, and Joao LL Rezende. A phase field concept for multiphase systems. *Physica D: Nonlinear Phenomena*, 94(3):135–147, 1996.

[107] Janin Tiaden, Britta Nestler, Hermann-Josef Diepers, and Ingo Steinbach. The multiphase-field model with an integrated concept for modelling solute diffusion. *Physica D: Nonlinear Phenomena*, 115(1-2):73–86, 1998.

[108] Balasubramaniam Radhakrishnan, Sarma B Gorti, John A Turner, Ranadip Acharya, John A Sharon, Alexander Staroselsky, and Tahany El-Wardany. Phase field simulations of microstructure evolution in in718 using a surrogate ni–fe–nb alloy during laser powder bed fusion. *Metals*, 9(1):14, 2019.

[109] Supriyo Ghosh, Kevin McReynolds, Jonathan E Guyer, and Dilip Banerjee. Simulation of temperature, stress and microstructure fields during laser deposition of ti–6al–4v. *Modelling and Simulation in Materials Science and Engineering*, 26(7):075005, 2018.

[110] Liang-Xing Lu, N Sridhar, and Yong-Wei Zhang. Phase field simulation of powder bed-based additive manufacturing. *Acta Materialia*, 144:801–809, 2018.

[111] Ranadip Acharya, John A Sharon, and Alexander Staroselsky. Prediction of microstructure in laser powder bed fusion process. *Acta Materialia*, 124:360–371, 2017.

[112] Trevor Keller, Greta Lindwall, Supriyo Ghosh, Li Ma, Brandon M Lane, Fan Zhang, Ursula R Kattner, Eric A Lass, Jarred C Heigel, Yaakov Idell, et al. Application of finite element, phase-field, and calphad-based methods to additive manufacturing of ni-based superalloys. *Acta materialia*, 139:244–253, 2017.

[113] Dehao Liu and Yan Wang. Mesoscale multi-physics simulation of solidification in selective laser melting process using a phase field and thermal lattice boltzmann model. In *International Design Engineering Technical Conferences and Computers and Information in Engineering Conference*, volume 58110, page V001T02A027. American Society of Mechanical Engineers, 2017.

[114] X Wang, PW Liu, Y Ji, Y Liu, MH Horstemeyer, and L Chen. Investigation on microsegregation of in718 alloy during additive manufacturing via integrated phase-field and finite-element modeling. *Journal of Materials Engineering and Performance*, 28(2):657–665, 2019.

[115] Linmin Wu and Jing Zhang. Phase field simulation of dendritic solidification of ti-6al-4v during additive manufacturing process. *JOM*, 70(10):2392–2399, 2018.

[116] Julia Kundin, Ali Ramazani, Ulrich Prahl, and Christian Haase. Microstructure evolution of binary and multicomponent manganese steels during selective laser melting: phase-field modeling and experimental validation. *Metallurgical and Materials Transactions A*, 50(4):2022–2040, 2019.

[117] M. Rappaz and Ch A. Gandin. Probabilistic modelling of microstructure formation in solidification processes. *Acta Metallurgica Et Materialia*, 41(2):345–360, 1993.

[118] Ch A. Gandin and M. Rappaz. A coupled finite element-cellular automaton model for the prediction of dendritic grain structures in solidification processes. *Acta Metallurgica Et Materialia*, 42(7):2233–2246, 1994.

[119] S Mishra and Tarasankar DebRoy. Measurements and monte carlo simulation of grain growth in the heat-affected zone of ti–6al–4v welds. *Acta Materialia*, 52(5):1183–1192, 2004.

[120] Tommy Carozzani, Ch-A Gandin, and Hugues Digonnet. Optimized parallel computing for cellular automaton–finite element modeling of solidification grain structures. *Modelling and Simulation in Materials Science and Engineering*, 22(1):015012, 2013.

[121] Stephen Wolfram. Cellular automata as models of complexity. *Nature*, 311(5985):419–424, 1984.

[122] Ch.-A Gandin and M Rappaz. A 3D Cellular Automaton algorithm for the prediction of dendritic grain growth. *Acta Materialia*, 45(5):2187–2195, may 1997.

[123] Ch-A Gandin, Michel Rappaz, and Rémy Tintillier. 3-dimensional simulation of the grain formation in investment castings. *Metallurgical and Materials Transactions A*, 25(3):629–635, 1994.

[124] Abha Rai, Harald Helmer, and Carolin Körner. Simulation of grain structure evolution during powder bed based additive manufacturing. *Additive Manufacturing*, 13:124–134, 2017.

[125] O. Zinovieva, A. Zinoviev, and V. Ploshikhin. Three-dimensional modeling of the microstructure evolution during metal additive manufacturing. *Computational Materials Science*, 141:207–220, 2018.

[126] Javed Akram, Pradeep Chalavadi, Deepankar Pal, and Brent Stucker. Understanding grain evolution in additive manufacturing through modeling. *Additive Manufacturing*, 21(March):255–268, 2018.

[127] Abha Rai, Matthias Markl, and Carolin Körner. A coupled Cellular Automaton–Lattice Boltzmann model for grain structure simulation during additive manufacturing. *Computational Materials Science*, 124:37–48, 2016.

[128] A. Zinoviev, O. Zinovieva, V. Ploshikhin, V. Romanova, and R. Balokhonov. Evolution of grain structure during laser additive manufacturing. Simulation by a cellular automata method. *Materials and Design*, 106:321–329, 2016.

[129] W. Wang, P. D. Lee, and M. McLean. A model of solidification microstructures in nickel-based superalloys: Predicting primary dendrite spacing selection. *Acta Materialia*, 51(10):2971–2987, 2003.

[130] H. B. Dong and P. D. Lee. Simulation of the columnar-to-equiaxed transition in directionally solidified Al-Cu alloys. *Acta Materialia*, 53(3):659–668, 2005.

[131] H. Yin and S. D. Felicelli. Dendrite growth simulation during solidification in the LENS process. *Acta Materialia*, 58(4):1455–1465, 2010.

[132] D. Tourret and A. Karma. Multiscale dendritic needle network model of alloy solidification. *Acta Materialia*, 61(17):6474–6491, 2013.

[133] D. Tourret and A. Karma. Three-dimensional dendritic needle network model for alloy solidification. *Acta Materialia*, 120:240–254, 2016.

[134] D. G. McCartney and J. D. Hunt. A Numerical Finite Difference Model of Steady State Cellular and Dendritic Growth. *Metallurgical Transactions A*, 15(6):983–994, 1984.

[135] J.D. Hunt and D.G. McCartney. Numerical finite difference model for steady state cellular array growth. *Acta Metallurgica*, 35(1):89–99, jan 1987.

[136] J. D. Hunt. A numerical analysis of dendritic and cellular growth of a pure material investigating the transition from "array" to "isolated" growth. *Acta Metallurgica Et Materialia*, 39(9):2117–2133, 1991.

[137] J. D. Hunt and Shu Zu Lu. Numerical modelling of cellular and dendritic array growth: spacing and structure predictions. *Materials Science and Engineering A*, 173(1-2):79–83, 1993.

[138] Suhas V Patankar. *Numerical heat transfer and fluid flow*. CRC press, 2018.

[139] Richard H Pletcher, John C Tannehill, and Dale Anderson. *Computational fluid mechanics and heat transfer*. CRC press, 2012.

[140] C.W Hirt and B.D Nichols. Volume of fluid (VOF) method for the dynamics of free boundaries. *Journal of Computational Physics*, 39(1):201–225, jan 1981.

[141] Vladimir D Liseikin. *Grid generation methods*, volume 1. Springer, 1999.

[142] Sergey Bochkanov. About alglib.

[143] Satish Balay, Shrirang Abhyankar, Mark F. Adams, Steven Benson, Jed Brown, Peter Brune, Kris Buschelman, Emil M. Constantinescu, Lisandro Dalcin, Alp Dener, Victor Eijkhout, William D. Gropp, Václav Hapla, Tobin Isaac, Pierre Jolivet, Dmitry Karpeev, Dinesh Kaushik, Matthew G. Knepley, Fande Kong, Scott Kruger, Dave A. May, Lois Curfman McInnes, Richard Tran Mills, Lawrence Mitchell, Todd Munson, Jose E. Roman, Karl Rupp, Patrick Sanan, Jason Sarich, Barry F. Smith, Stefano Zampini, Hong Zhang, Hong Zhang, and Junchao Zhang. PETSc Web page. `https://petsc.org/`, 2021.

[144] Satish Balay, Shrirang Abhyankar, Mark F. Adams, Steven Benson, Jed Brown, Peter Brune, Kris Buschelman, Emil Constantinescu, Lisandro Dalcin, Alp Dener, Victor Eijkhout, William D. Gropp, Václav Hapla, Tobin Isaac, Pierre Jolivet, Dmitry Karpeev, Dinesh Kaushik, Matthew G. Knepley, Fande Kong, Scott Kruger, Dave A. May, Lois Curfman McInnes, Richard Tran Mills, Lawrence Mitchell, Todd Munson, Jose E. Roman, Karl Rupp, Patrick Sanan, Jason Sarich, Barry F. Smith, Stefano Zampini, Hong Zhang, Hong Zhang, and Junchao Zhang. PETSc/TAO users manual. Technical Report ANL-21/39 - Revision 3.16, Argonne National Laboratory, 2021.

[145] Satish Balay, William D. Gropp, Lois Curfman McInnes, and Barry F. Smith. Efficient management of parallelism in object oriented numerical software libraries. In E. Arge, A. M. Bruaset, and H. P. Langtangen, editors, *Modern Software Tools in Scientific Computing*, pages 163–202. Birkhäuser Press, 1997.

[146] John E Dennis Jr and Robert B Schnabel. *Numerical methods for unconstrained optimization and nonlinear equations*. SIAM, 1996.

[147] Hisham M. Ettouney and Robert A. Brown. Finite-element methods for steady solidification problems. *Journal of Computational Physics*, 49(1):118–150, 1983.

[148] G. Boussinot, M. Apel, J. Zielinski, U. Hecht, and J. H. Schleifenbaum. Strongly Out-of-Equilibrium Columnar Solidification during Laser Powder-Bed Fusion in Additive Manufacturing. *Physical Review Applied*, 11(1):1, 2019.

[149] Doru Michael Stefanescu. *Science and engineering of casting solidification*. Springer, 2015.